

Omnidirectional Energetic Electron Fluxes from 150 km to 20,000 km: an ELFIN-Based Model

Emile Saint-Girons^{1,2}, Xiao-Jia Zhang^{1,3}, Didier Mourenas^{4,5}, Anton V. Artemyev³, Vassilis Angelopoulos³

¹Department of Physics, University of Texas at Dallas, Richardson, Texas, USA

²CentraleSupélec, Gif-sur-Yvette, France

³Department of Earth, Planetary, and Space Sciences, University of California, Los Angeles, Los Angeles, California, USA

⁴CEA, DAM, DIF, Arpaion, France

⁵Laboratoire Matière en Conditions Extrêmes, Université Paris-Saclay, CEA, Bruyères-le-Châtel, France

Key Points:

- Quasi-linear theory is used to infer omnidirectional electron flux along magnetic field lines from low-altitude spacecraft measurements
- The obtained analytical model of average omnidirectional electron flux is consistent with equatorial measurements from the Van Allen Probes
- The model shows the impact of impulsive and time-integrated geomagnetic activity on electron fluxes in plasma sheet and outer radiation belt

arXiv:2406.05579v2 [physics.space-ph] 19 Jun 2024

Corresponding author: Xiao-Jia Zhang, xjzhang@utdallas.edu

Abstract

The strong variations of energetic electron fluxes in the Earth’s inner magnetosphere are notoriously hard to forecast. Developing accurate empirical models of electron fluxes from low to high altitudes at all latitudes is therefore useful to improve our understanding of flux variations and to assess radiation hazards for spacecraft systems. In the present work, energy- and pitch-angle-resolved precipitating, trapped, and backscattered electron fluxes measured at low altitude by Electron Loss and Fields Investigation (ELFIN) CubeSats are used to infer omnidirectional fluxes at altitudes below and above the spacecraft, from 150 km to 20,000 km, making use of adiabatic transport theory and quasi-linear diffusion theory. The inferred fluxes are fitted as a function of selected parameters using a stepwise multivariate optimization procedure, providing an analytical model of omnidirectional electron flux along each geomagnetic field line, based on measurements from only one spacecraft in low Earth orbit. The modeled electron fluxes are provided as a function of L -shell, altitude, energy, and two different indices of past geomagnetic activity, computed over the preceding 4 hours or 3 days, potentially allowing to disentangle impulsive processes (such as rapid injections) from cumulative processes (such as inward radial diffusion and wave-driven energization). The model is validated through comparisons with equatorial measurements from the Van Allen Probes, demonstrating the broad applicability of the present method. The model indicates that both impulsive and time-integrated geomagnetic activity partly control electron fluxes in the outer radiation belt and in the plasma sheet.

1 Introduction

The high variability of electron fluxes trapped along geomagnetic field lines in the Earth’s inner magnetosphere has been a focus of intense research since the discovery of the radiation belts, both to improve our fundamental understanding of the space environment and as a practical necessity to mitigate space weather hazards for satellites (Li & Hudson, 2019; Zheng et al., 2019). Energetic electron fluxes in the outer radiation belt (at McIlwain shells $L \geq 3-4$) vary both spatially and temporally, exhibiting steep increases after prolonged periods of high geomagnetic activity corresponding to plasma sheet injections accompanied by wave-driven electron energization (Hua et al., 2022; Mourenas et al., 2019, 2023), as well as sudden dropouts mainly caused by solar wind dynamic pressure impulses and magnetopause shadowing (Boynnton et al., 2017; Shprits et al., 2006). Electron precipitation through resonant interactions with whistler-mode waves or electromagnetic ion cyclotron (EMIC) waves can lead to fast losses (Mourenas et al., 2017; Ross et al., 2021), while electron energization by whistler-mode chorus waves, or through radial transport by ULF waves, can increase trapped fluxes by orders of magnitude over a typical time scale of a few days (Horne et al., 2005; Mourenas et al., 2023; Ozeke et al., 2014; Thorne et al., 2013). Flux variations with magnetic local time (MLT) can also be significant, depending on geomagnetic activity (Allison et al., 2017; Meredith et al., 2016).

The balance between electron flux injections and losses depends on a number of factors, such as the level of geomagnetic activity, the solar wind speed and dynamic pressure and the local plasma density, which can all modify the strength of the different physical processes at work. Such physical processes also affect the equatorial pitch-angle distribution of electrons and the corresponding flux distribution along magnetic field lines (Kennel & Petschek, 1966; Li et al., 2013; Mourenas et al., 2014). Therefore, developing a model of the distribution of omnidirectional electron fluxes along fixed geomagnetic field lines as a function of L , MLT, and geomagnetic activity can be useful for assessing the dominant physical processes at a given time and location.

Besides, internal charging represents a major hazard for satellites (Chen et al., 2021; Zheng et al., 2019). It is caused by high fluxes of energetic to relativistic (> 200 keV)

electrons. The total dose of such radiation can be used to estimate the charge deposition inside spacecraft electronic components and the probability of electrostatic discharges in dielectrics. Increases in lower energy $\sim 1\text{--}200$ keV electron fluxes can similarly lead to satellite surface charging, potentially resulting in electrostatic discharges that may damage solar array panels (Zheng et al., 2019). Therefore, it is crucial for spacecraft designers to estimate the total radiation dose expected during a satellite lifetime (Zheng et al., 2019). Spacecraft operators also need predictive (or probabilistic) models with a capability to forecast periods of particularly elevated electron fluxes, which may allow mitigating the impact of space weather hazards – for instance, by temporarily shutting down satellite operations.

While various past models of radiation belt electron fluxes (e.g., see Boynton et al., 2016; Simms et al., 2023, and references therein) have focused on geosynchronous orbit (GEO), the total ionizing dose risks for satellites in Low Earth Orbit (LEO), Highly Elliptical Orbit (HEO), and Medium Earth Orbit (MEO), are somewhat less well known. Electron fluxes have been found to vary coherently from LEO to higher altitudes on the same L -shell at $L \leq 7$ (Kanekal et al., 2001; Shane et al., 2023). Building on this coherency, various machine learning models have recently been developed to nowcast or forecast the electron flux at LEO, HEO, MEO, and GEO, based on conjugate measurements of electron fluxes by LEO or Global Positioning System (GPS) spacecraft and several solar wind or geomagnetic indices (Boyd et al., 2023; Pires de Lima et al., 2020; Smirnov et al., 2020). Other recent models provide deterministic or probabilistic forecasts of the electron flux at different orbits, based only on past solar wind or geomagnetic indices, the expected future level of such indices, or sequences of time-integrated values of past geomagnetic indices (Boynton et al., 2019; D. Ma et al., 2022; Mourenas, Agapitov, et al., 2022; Simms et al., 2023).

In the present work, the full dataset of electron fluxes measured by Electron Loss and Fields Investigation (ELFIN) CubeSats (Angelopoulos et al., 2020) at low altitude (~ 450 km) in 2020–2022 is used to develop a model of omnidirectional 60 – 1500 keV electron fluxes, at altitudes varying from 150 km to 20,000 km along L -shells ranging from $L = 1.5$ to $L = 10$, as a function of past geomagnetic activity. Making use of adiabatic transport theory and quasi-linear diffusion theory, we provide a self-consistent model of omnidirectional electron flux, solely based on measurements in low Earth orbit. Problems related to conjunction and intercalibration uncertainties arising when combining data from different spacecraft on different orbits are naturally avoided, resulting in inferred electron fluxes intrinsically coherent at all altitudes along a given geomagnetic field line. Stepwise regression is used to obtain an analytical model of electron flux based on inferred fluxes. Simms et al. (2023) have shown that electron flux models obtained through stepwise regression procedures can reach roughly similar accuracy and predictive ability as neural network models, while being simpler and more portable. In the present model, average electron fluxes are provided for four different ranges of two different indices of past geomagnetic activity, over the preceding 4 hours or over the previous 72 hours.

Hereafter, Section 2 describes the methodology employed to infer omnidirectional electron fluxes at various altitudes along a given geomagnetic field line from ELFIN measurements of pitch-angle resolved electron fluxes at 450 km altitude. The stepwise optimization procedure and the resulting analytical model of omnidirectional electron flux are described in Section 3. In Section 4, the model is validated by comparisons with other spacecraft measurements near the magnetic equator, and several physical implications of the results are discussed.

2 Methods and Data

2.1 ELFIN Dataset

In the following, ELFIN CubeSats (referred to respectively as ELFIN-A and ELFIN-B) measurements of 60–1500 keV precipitating, trapped (or quasi-trapped), and backscattered electron fluxes (Angelopoulos et al., 2020) at 400 – 450 km altitude are used to develop a novel model of omnidirectional electron fluxes at all altitudes along each geomagnetic field line, down to 150 km altitude below ELFIN and up to $\sim 20,000$ km altitude above it, making use of adiabatic transport theory and quasi-linear diffusion theory. The two CubeSats were launched in a nearly polar circular orbit of 90 minutes period. They have provided energy and pitch-angle resolved measurements of electron fluxes during the spacecraft spin period of 2.85 seconds, from 2019 to 2022. The energy resolution is $\Delta E/E \sim 40\%$ and the resolution in local pitch-angle α is $\Delta\alpha \sim 22.5^\circ$ from $\alpha = 0^\circ$ to $\alpha = 360^\circ$. This data set has been used in various recent studies to investigate wave-particle interactions and their effects on electron fluxes and has been described extensively in previous papers (e.g., see Angelopoulos et al., 2023; Mourenas et al., 2021, 2023; Zhang, Artemyev, et al., 2022).

In the present study, the 2020-2022 datasets of ELFIN A and B are used, representing respectively 5,200 and 4,100 separate time periods (each period is one ELFIN orbit or so-called *science zone*; see Tsai et al., 2024) with available data, with a mean duration of 8 min. Two different parameters, AE^* and AE^{**} , are used to quantify geomagnetic activity. The AE^* index (in nT) is defined as the mean value of the AE index during the previous 4 hours, allowing to roughly take into account the expected travel time of $\sim 10 - 100$ keV electrons injected from the plasma sheet in the midnight sector before they can locally generate whistler-mode waves and provide a seed electron population that can be accelerated to higher energies. Hereafter, the SuperMAG SME index is employed as a fair proxy for the AE index (Gjerloev, 2012). The AE^{**} index (in nT·hr), defined as the time-integrated AE (or SME) during the preceding 72 hours, is used to take into account the peculiar effects of high time-integrated geomagnetic activity (i.e., of prolonged injections, ULF wave-driven radial diffusion and electron energization, and chorus wave-driven electron acceleration), which are known to produce the highest omnidirectional electron fluxes in the outer radiation belt (Hua et al., 2022; Mourenas et al., 2019; Mourenas, Agapitov, et al., 2022). These two different parameters, AE^* and AE^{**} , can therefore be used to separate the effects of rapid physical processes from those of prolonged cumulative processes in electron flux variations.

2.2 Omnidirectional Electron Flux at Altitudes Lower than ELFIN

Firstly, ELFIN measurements at an altitude $h_0 \sim 450$ km of pitch-angle resolved (i.e. directional) differential electron fluxes $J(h_0, \alpha_{h_0}, E)$, in units of $\text{e}/\text{cm}^2/\text{s}/\text{sr}/\text{MeV}$, with α_{h_0} the local pitch-angle, are used to infer omnidirectional fluxes $J_{\text{omni}}(h, E)$ at $h \leq h_0$, down to $h = 150$ km below the spacecraft. For equipotential magnetic field lines and slow variations of the near-Earth geomagnetic field compared to an electron gyroperiod, the conservation of the number and energy of electrons and of the magnetic flux and first adiabatic invariant between h_0 and h along the same field line leads to the conservation of the gyrotropic unidirectional flux, $J(h, \alpha_h(\alpha_{h_0}), E) = J(h_0, \alpha_{h_0}, E)$ (Roederer, 1970; Schulz & Lanzerotti, 1974; Walt, 1994). The omnidirectional differential electron flux (in $\text{e}/\text{cm}^2/\text{s}/\text{MeV}$) at h_0 is given by

$$J_{\text{omni}}(h_0, E) = 2\pi \int_0^\pi J(h_0, \alpha_{h_0}, E) \sin \alpha_{h_0} d\alpha_{h_0}. \quad (1)$$

For the sake of simplicity, we hereafter use an eccentric (off-centered) and inclined dipolar external geomagnetic field model (e.g., see Koochak & Fraser-Smith, 2017), which is a reasonable approximation to the actual geomagnetic field for $h \in [150; 20,000]$ km, together with the International Geomagnetic Reference Field (IGRF; see Thébault et

al., 2015) magnetic latitude of the spacecraft provided in the ELFIN data set. The downward part of the omnidirectional flux, J_{omni}^{down} , at an altitude $h < h_0$ on the same field line as ELFIN can then be written as

$$J_{omni}^{down}(h, E) = 2\pi \int_0^{\alpha_{max,0}} J(h, \alpha_h(\alpha_{h_0}), E) \sin \alpha_h(\alpha_{h_0}) \frac{\partial \alpha_h}{\partial \alpha_{h_0}} d\alpha_{h_0}, \quad (2)$$

where $\alpha_{max,0}$, the local pitch-angle at h_0 , corresponds to a local pitch-angle $\alpha_h = \pi/2$ at h (Ni et al., 2009). Conservation of the first adiabatic invariant yields $\sin^2 \alpha_h / \sin^2 \alpha_{h_0} = B(h)/B(h_0)$, with $B(h)$ the geomagnetic field strength (Roederer, 1970; Schulz & Lanzerotti, 1974), giving $\sin \alpha_{h_0} \leq \sin \alpha_h$ for $h \leq h_0$. Therefore, $J_{omni}(h, E)$ at $h \leq h_0$ is fully determined by $J(h_0, \alpha_{h_0}, E)$ at h_0 together with conservation of unidirectional flux, energy, and first adiabatic invariant. Since $\partial \alpha_h / \partial \alpha_{h_0} = B(h) \sin \alpha_{h_0} \cos \alpha_{h_0} / (B(h_0) \sin \alpha_h \cos \alpha_h)$, this finally gives:

$$J_{omni}^{down}(h, E) = 2\pi \frac{B(h)}{B(h_0)} \int_0^{\alpha_{max,0}} J(h_0, \alpha_{h_0}, E) \frac{\sin \alpha_{h_0} \cos \alpha_{h_0}}{\sqrt{1 - \frac{B(h)}{B(h_0)} \sin^2 \alpha_{h_0}}} d\alpha_{h_0}, \quad (3)$$

where $J(h_0, \alpha_{h_0}, E)$ is the directional differential flux inferred, by cubic spline interpolation, from the fluxes measured by ELFIN on different pitch-angle intervals ($B(h)/B(h_0)$ is evaluated for an inclined eccentric dipolar geomagnetic field). The integral in Equation (3) is calculated using the QUAD package from the Scientific Python (SciPy) library, which allows to smoothly take into account a singularity at $\alpha_h = \pi/2$. The upward omnidirectional flux $J_{omni}^{up}(h, E)$ is similarly obtained from the (upward) directional flux at $\alpha_{h_0} \in [\pi/2, \pi]$ measured by ELFIN, and the total omnidirectional electron flux is $J_{omni} = J_{omni}^{down} + J_{omni}^{up}$.

2.3 Omnidirectional Electron Flux at Altitudes Higher than ELFIN

In several previous works, equatorial electron fluxes at high altitudes have been inferred from low-altitude flux measurements based on the observed high correlations between conjugate low-altitude and high-altitude fluxes, or else by using statistical pitch-angle distributions from the Van Allen Probes (Allison et al., 2018; Pires de Lima et al., 2020; Boyd et al., 2023). In the present study, we adopt a different approach. At altitudes $h \geq h_0$, the part of the omnidirectional flux at $\alpha_h \in [0, \alpha_{hAL}]$ and at $\alpha_h \in [\pi - \alpha_{hAL}, \pi]$, with α_{hAL} the adiabatic limit (AL) at h corresponding to $\alpha_{h_0} = \pi/2$ on the same field line, can still be directly inferred from ELFIN measurements using adiabatic transport theory, as in Section 2.2. However, this part of $J_{omni}(h, E)$ becomes smaller and smaller at higher altitudes because α_{hAL} decreases as h increases above h_0 .

Assuming that a quasi-equilibrium pitch-angle electron distribution has been reached after hours to days of wave-particle interactions (for justifications of this assumption, see Mourenas et al., 2021; Shane et al., 2023), we therefore use quasi-linear diffusion theory (Kennel & Petschek, 1966; Li et al., 2013) to infer high-altitude fluxes at local pitch-angles $\alpha_h \in [\alpha_{hAL}, \pi - \alpha_{hAL}]$ from low-altitude fluxes measured by ELFIN. This is achieved with the help of simultaneous ELFIN measurements of the net precipitating to trapped flux ratio, J_{prec}/J_{trap} . As in previous works, the net precipitating flux, J_{prec} , directly precipitated by wave-particle interactions, is defined as the measured precipitating flux averaged inside the local bounce loss cone, minus the average upward flux J_{up} backscattered inside the same bounce loss cone, where J_{up} is used as a proxy for the flux backscattered by the atmosphere from the opposite hemisphere on the same field line over times long compared to a bounce period (Mourenas et al., 2021, 2023). This estimate of the net precipitating to trapped flux ratio J_{prec}/J_{trap} relies on the assumption that a majority of backscattered electrons should remain within the same energy bin of width $\Delta E/E \approx 40\%$ (in agreement with simulations, see Marshall & Bortnik, 2018; Selesnick et al., 2004) and also assumes a symmetric system about the magnetic equator. But since random errors should partly cancel out after averaging the inferred high altitude fluxes over many

measurements at various locations, the estimated time-averaged high altitude flux should remain approximately correct in the presence of small deviations from symmetry.

At $L \sim 1.5\text{--}10$ in the inner magnetosphere and near-Earth plasma sheet, in the presence of typical populations of incoherent whistler-mode waves or of mostly short and intense whistler-mode wave packets with random frequency and phase jumps (Gao et al., 2022; He et al., 2021; Mourenas, Zhang, et al., 2022; Zhang, Agapitov, et al., 2020; Zhang, Mourenas, et al., 2020), the quasi-linear diffusion theory is expected to remain approximately valid (Artemyev et al., 2022; Mourenas et al., 2021; Mourenas, Zhang, et al., 2022; Zhang, Agapitov, et al., 2020). Quasi-linear theory probably also holds in the presence of other types of waves with similar characteristics, such as EMIC waves (Angelopoulos et al., 2023; Remya et al., 2017).

Quasi-linear diffusion theory (Kennel & Petschek, 1966) provides an approximate relationship between the effective pitch-angle diffusion rate $D_{\alpha\alpha}$ of electrons at the loss cone angle and the average net precipitating to trapped flux ratio J_{prec}/J_{trap} measured at ELFIN CubeSats (Mourenas et al., 2023, 2024):

$$z_0 \simeq \left(10^4 + 260 \frac{J_{trap}}{J_{prec}}\right)^{1/2} - 100, \quad (4)$$

with a moderate error $< 25\%$ for $J_{prec}/J_{trap} < 0.85$, $z_0 = 2\alpha_{eq,LC}/(D_{\alpha\alpha}\tau_B)^{1/2}$, $\tau_B(E, L)$ the electron bounce period, and where $D_{\alpha\alpha}(E, L)$ is calculated at the equatorial loss cone angle $\alpha_{eq,LC}$, which corresponds to a local $\alpha = \pi/2$ at $h = 100$ km (Schulz & Lanzerotti, 1974). The average quasi-equilibrium directional electron flux at $\alpha_h > \alpha_{hAL}$ is given by quasi-linear theory (Kennel & Petschek, 1966; Mourenas et al., 2024):

$$\frac{J(h, \alpha_h, E)}{J(h, \alpha_{hAL}, E)} \approx \frac{1 + z_0 \frac{I_1(z_0)}{I_0(z_0)} \ln\left(\frac{\sin \alpha_{eq,h}}{\sin \alpha_{eq,LC}}\right)}{1 + z_0 \frac{I_1(z_0)}{I_0(z_0)} \ln\left(\frac{\sin \alpha_{eq,hAL}}{\sin \alpha_{eq,LC}}\right)}, \quad (5)$$

where I_x is the modified Bessel function of the first kind, and $\alpha_{eq,h}$ and $\alpha_{eq,hAL}$ are the equatorial pitch-angles corresponding to α_h and α_{hAL} , respectively. Using Equations (4) and (5), the directional electron flux at $\alpha_h \in [\alpha_{hAL}, \pi/2]$ can be inferred from ELFIN measurements of J_{prec}/J_{trap} and $J(h_0, \alpha_{h_0} = \pi/2, E) = J(h, \alpha_{hAL}, E)$. We also assume that $J(h, \pi - \alpha_h, E) \simeq J(h, \alpha_h, E)$ to first order for $\alpha_h \in [\pi/2, \pi - \alpha_{hAL}]$. This assumption is justified for a roughly symmetric system about the magnetic equator, especially for J_{omni} since integrating over all pitch-angles reduces the average relative error. The total omnidirectional flux $J_{omni}(h, E)$ is finally obtained by summing two parts: a first, adiabatic part at $\alpha_h < \alpha_{hAL}$ and $\alpha_h > \pi - \alpha_{hAL}$ calculated as in Section 2.2, and a second part calculated over the remaining α_h range by integrating as in Equation (1) the directional fluxes obtained from Equation (5).

Note that the above method is valid only when $J_{prec}/J_{trap} < 0.85$, that is, in a regime of weak diffusion. When $J_{prec}/J_{trap} > 0.85$, we enter a regime of strong diffusion, where $z_0 \simeq 1$ (Kennel, 1969). Equation (5) indicates that for $z_0 = 1$, $J(h, \alpha_h, E)$ increases only very weakly as α_h increases. In the strong diffusion regime, the actual $D_{\alpha\alpha}$ can even exceed the theoretical level corresponding to $z_0 = 1$, leading to a constant $J(h, \alpha_h, E)$ at $\alpha_h > \alpha_{hAL}$. When $J_{prec}/J_{trap} > 0.85$, it is therefore reasonable to use the simple approximation $J(h, \alpha_h, E) \approx J(h, \alpha_{hAL}, E)$ for $\alpha_h > \alpha_{hAL}$, with a corresponding error on $J(h, \alpha_h, E)$ usually much smaller than a factor of 2.

2.4 Expected Validity Domain

Some limitations of the present method for inferring fluxes at $h > h_0$ are worth mentioning. Equation (5) has been derived by assuming, as in the original work by Kennel and Petschek (1966), that $D_{\alpha\alpha}$ is varying with α_{eq} roughly like $\approx 1/\cos \alpha_{eq}$ at $\alpha_{eq} <$

$80^\circ - 90^\circ$. Analytical estimates, validated by numerical simulations, have shown that for quasi-parallel whistler-mode waves, the actual variation of $D_{\alpha\alpha}$ with α_{eq} is usually closer to $\approx 1/\cos^2 \alpha_{eq}$ above ~ 100 keV (Agapitov et al., 2018; Artemyev, Mourenas, et al., 2013; Li et al., 2015; Mourenas et al., 2012). However, depending on wave power and frequency distributions and plasma density, the variation of $D_{\alpha\alpha}$ may sometimes become similar to $\approx \cos \alpha_{eq}$, especially at $L < 3.5$ and low energy (Green et al., 2020; Li et al., 2015; Q. Ma et al., 2017, 2022). For these two alternative variations of $D_{\alpha\alpha}$ with α_{eq} , all terms of the form $\ln(\sin \alpha_{eq})$ in Equation (5) have to be replaced, in the first case by $\cos \alpha_{eq} + \ln(\tan(\alpha_{eq}/2))$, and in the second case by $\ln(\tan \alpha_{eq})$. In a dipolar geomagnetic field at $L > 1.5$, $J_{omni}(h, E)$ values inferred using Equation (5) at $\alpha_{eq} < 80^\circ - 85^\circ$ (assuming the same variation of $D_{\alpha\alpha}$ with α_{eq} as Kennel & Petschek, 1966) remain within a factor of $\approx 1.5-2$ from $J_{omni}(h, E)$ values inferred using the above-discussed two alternative variations of $D_{\alpha\alpha}$ with α_{eq} , indicating the reliability of Equation (5).

However, the eccentric dipole approximation to the actual geomagnetic field remains reasonable only up to $h \approx 20,000$ km during disturbed periods (e.g., see Berube et al., 2006; Roederer & Lejosne, 2018). This suggests that the accuracy of the $J_{omni}(h, E)$ model should be ensured only for

$$h < h_{max} \approx 20,000 \text{ km.} \quad (6)$$

This maximum altitude h_{max} corresponds to maximum equatorial pitch-angles $\alpha_{eq,max} \sim \sin^{-1} \left((1 + h_{max}/R_E)^{3/2} / (L^{3/2}(4 - 3(1 + h_{max}/R_E)/L)^{1/4}) \right)$ for the applicability of the present method, giving $\alpha_{eq,max} \lesssim 70^\circ, 45^\circ$, and 25° at $L > 4, 5$ and 6 , respectively.

In addition, the variation of $D_{\alpha\alpha}$ with α_{eq} can sometimes be more complex than the above-discussed simple scaling laws. But taking into account all waves (and Coulomb collisions) at $L = 1.5 - 6$ within the plasmasphere or in a plasmaspheric plume, $D_{\alpha\alpha}$ should usually not decrease by much more than a factor of $\sim \tan \alpha_{eq,LC} / \tan \alpha_{eq}$ as α_{eq} increases from $\alpha_{eq,LC}$ to $\alpha_{eq,max} = \alpha_{eq}(h_{max})$ for $0.1-1.5$ MeV electrons (Angelopoulos et al., 2023; Green et al., 2020; Li et al., 2015; Q. Ma et al., 2017, 2022; X. Shi et al., 2024; Wong et al., 2022). Then, the inferred $J_{omni}(h, E)$ should remain within a factor of ≈ 2 from the actual $J_{omni}(h, E)$ at $h < h_{max}$.

Outside the plasmasphere, chorus wave-driven energy diffusion can compete with pitch-angle diffusion (Horne et al., 2005; Summers et al., 1998), but Van Allen Probes observations show that this should not significantly modify the increase of $J(\alpha_{eq})$ with α_{eq} up to at least $\alpha_{eq} \approx 50^\circ$ for $E < 1.5$ MeV (Li et al., 2014). At $L \sim 6 - 10$, magnetic field line curvature scattering (Young et al., 2002) still leads to an increase of $D_{\alpha\alpha}$ up to $\alpha_{eq,max} = \alpha_{eq}(h_{max})$ (Artemyev, Orlova, et al., 2013), and drift shell splitting should not strongly modify $J(\alpha_{eq})$ below $\alpha_{eq}(h_{max})$ (Selesnick & Blake, 2002), which should keep the inferred $J_{omni}(h, E)$ within a factor of ~ 1.5 from the actual $J_{omni}(h, E)$ at $h < h_{max}$.

Finally, it is worth emphasizing that our model of omnidirectional electron flux is based on time-averaged inferred fluxes J_{omni} , averaged inside each parameter bin over at least 25 (and often much more) ELFIN measurements performed at different times. Random errors on individual inferred J_{omni} values will partly cancel each other out. Therefore, the average inferred $J_{omni}(h < h_{max}, E)$ is expected to remain less than a factor of ~ 1.5 (at $L > 3.5$) to ~ 2 (at $L < 3.5$) from the actual average $J_{omni}(h, E)$.

3 Model of Omnidirectional Electron Fluxes

3.1 Data Selection

The electron detector onboard ELFIN Cubesats provides differential electron fluxes measured in 16 logarithmically spaced energy channels (each with a full width of $\Delta E/E \sim 40\%$) whose central values extend from 60 keV to 6.5 MeV (Angelopoulos et al., 2020).

Over a spacecraft spin period of 2.85 s, an ELFIN CubeSat provides two complete electron flux measurements of the entire 180° local pitch-angle distribution, with a $\sim 22.5^\circ$ resolution, resolving quasi-trapped, precipitating, and upward-moving electrons backscattered by the atmosphere (Angelopoulos et al., 2020).

Before computing J_{omni} , a strict data screening procedure is used in order to only keep the most reliable electron flux data:

- firstly, if $J(\alpha_{h_0}) < 100 \text{ e/cm}^2/\text{s}/\text{sr}/\text{MeV}$ at a given pitch-angle, or if the associated number of counts per second is below 5 for a given channel, the measured flux is considered to be null for this channel, in order to only keep fluxes above instrument noise level (Mourenas et al., 2024). This conservative approach should only lead to a very slight underestimation of the final time-averaged omnidirectional flux, since such cases correspond to very low to null fluxes, much smaller than retained fluxes,
- at a given time, for a given energy channel, at least three pitch-angle bins must be associated with non-zero fluxes,
- if there are exactly three pitch-angle bins associated with non-zero fluxes, they must be adjacent pitch-angles (to exclude fluxes with abnormal fluctuations),
- the flux measured at the first pitch-angle just above the loss cone angle must be non-zero (to have a non-null quasi-trapped flux) and higher than the flux measured just below (opposite cases may correspond to occasional rapid fluctuations or to isolated bursts of very oblique waves leading to a fully nonlinear electron transport that cannot be described by quasi-linear theory, see Zhang, Artemyev, et al., 2022).

We then compute, for acceptable measurements, the time-averaged corresponding values of J_{prec} and J_{trap} , discarding cases for which one of these values turns out to be non-positive or not calculable. As a result, about 20% of the full 2020-2022 ELFIN data set have been retained, the overwhelming majority of data rejections being due to the presence of less than three pitch-angles with non-zero flux at a given time and at a given energy.

Finally, the omnidirectional fluxes $J_{omni}(h, E, L)$ are inferred from ELFIN data at 18 pre-determined altitudes between $h = 150 \text{ km}$ and $h = 20,000 \text{ km}$ (at 150, 200, 250, 350, 450, 600, 800, 1000, 1200, 1600, 2000, 4000, 6000, 8000, 11000, 14000, 17000, 20000 km), with a shorter step at lower altitudes where flux variations are stronger, and for $E \in [0.06, 1.5] \text{ MeV}$ and $L \in [1.5, 10]$ using the methods described in Section 2. It is worth noticing that the values of J_{prec} and J_{trap} used to compute the net precipitating to trapped flux ratio (necessary to establish the weak diffusion condition, and then considered in Equation 4 and, for J_{trap} , in the denominator of the left-hand side of Equation 5) are averaged on all positive available values over a 18-second sliding window, to provide more reliable fluxes, time-averaged over a period much longer than a bounce period (Mourenas et al., 2021), also mitigating possible time aliasing effects (Angelopoulos et al., 2023; Zhang, Angelopoulos, et al., 2022).

We use ELFIN A data as the training subset, and ELFIN B data as a validation subset. For each subset, omnidirectional fluxes are averaged inside each parameter bin (AE^*, E, L, h) or (AE^{**}, E, L, h) . To do so, L is rounded to the nearest quarter of an integer, and AE^* and AE^{**} values are each associated to one of the four following levels of instantaneous or time-integrated geomagnetic activity:

- quiet (AE_0^* and AE_0^{**} levels): $AE^* < 100 \text{ nT}$ or $AE^{**} < 10^4 \text{ nT}\cdot\text{h}$
- moderate (AE_1^* and AE_1^{**} levels): $100 \text{ nT} < AE^* < 300 \text{ nT}$ or $10^4 \text{ nT}\cdot\text{h} < AE^{**} < 2 \cdot 10^4 \text{ nT}\cdot\text{h}$

- active (AE_2^* and AE_2^{**} levels): $300 \text{ nT} < AE^* < 500 \text{ nT}$ or $2 \cdot 10^4 \text{ nT} \cdot \text{h} < AE^{**} < 3 \cdot 10^4 \text{ nT} \cdot \text{h}$
- very active (AE_3^* and AE_3^{**} levels): $AE^* > 500 \text{ nT}$ or $AE^{**} > 3 \cdot 10^4 \text{ nT} \cdot \text{h}$.

We obtain that way, for each subset, a time-averaged profile of the flux as a function of altitude, $J_{omni}(h)$, for each (E, L, AE_i^*) and (E, L, AE_i^{**}) , where h is varying from 150 km up to a maximum altitude that depends on L -shell and does not exceed 20,000 km.

We finally perform a last sorting, by:

- discarding values of $J_{omni}(h)$ averaged over less than 25 instantaneous values (each averaged value of $J_{omni}(h)$ considered thereafter will that way be temporally averaged over at least 36 s, since ELFIN gives two measurements of the full 180° pitch-angle domain per spin of 2.85 s),
- next, deleting whole $J_{omni}(h)$ profiles in altitude with less than four values of $J_{omni}(h)$ at $h > h_0$ (which concretely imposes, given the set of altitudes considered, a maximum altitude $h \geq 1,200$ km for an averaged $J_{omni}(h)$ profile to be taken into account),
- deleting the few $J_{omni}(h)$ profiles for which $J_{omni}(h)$ decreases by more than 5% just above h_0 (probably due to a drop in the number of $J_{omni}(h)$ values taken into account in the calculation of the average, since $J_{omni}(h)$ is sometimes available only at $h \leq h_0$ due to the impossibility of applying the weak or strong diffusion approximations mentioned above),
- deleting $J_{omni}(h)$ profiles associated to an energy higher than 1.5 MeV (such profiles are rare and the corresponding average J_{omni} values are calculated based on only few values),
- deleting the small number of average inferred $J_{omni}(E, L, h)$ profiles with values lower than $300 \text{ e/cm}^2/\text{s/MeV}$ at $h = 450$ km, because they are much lower than all the others and mostly correspond to noise.

Note that ELFIN regular *science zones* (Tsai et al., 2024) mostly cover $L \sim 3 - 12$, whereas data from lower L -shells are much more sparse. Therefore, all the average inferred $J_{omni}(E, L, h)$ profiles at $L \in [1.5, 3.5]$, much rarer than at $L \in [3.5, 10]$, are regrouped in one set independently of the AE level. This procedure, necessary to obtain reliable values for all (E, L) pairs, is justified by the weaker variation of time-averaged 0.06 – 1.5 MeV electron fluxes with geomagnetic activity at $L \leq 3$ than at $L > 3.5$ (e.g., see Mourenas et al., 2017; Reeves et al., 2016). As a result, however, the model includes no dependence on geomagnetic activity at $L \in [1.5, 3.5]$.

We finally get, for each geomagnetic activity indicator, a training data set, derived from ELFIN A measurements, and a validation data set, derived from ELFIN B measurements, consisting each of 1200 $J_{omni}(h)$ profiles for both AE^* and AE^{**} .

3.2 Multivariate Optimization Analysis of Electron Flux Variations

In this section, multivariate optimization analysis (Gill et al., 2020) is used for specifying a model of omnidirectional electron flux $J_{omni}(h, E, L)$ as a function of altitude (h), energy (E), and L , for the four aforementioned levels of preceding geomagnetic activity (defined by AE^* or AE^{**} parameters), based on J_{omni} values inferred from ELFIN electron flux data collected in 2020-2022. We first examine $J_{omni}(h, E, L)$ values averaged over MLT, to obtain a much larger number of data points in each parameter bin, and also because past studies have shown that the variations of electron flux with MLT usually remain moderate (a factor of ≈ 2 between dawn and dusk for $AE^* < 1000$ nT, see Allison et al., 2017; Meredith et al., 2016). The electron equatorial pitch-angle distribution, formed by wave-particle interactions over many azimuthal drift periods (Schulz

& Lanzerotti, 1974), also remains roughly similar at all MLTs at $L \sim 1.5 - 6$ during not-too-disturbed periods (R. Shi et al., 2016). The MLT variations of J_{omni} will nevertheless be examined further below.

The three independent variables h , E , and L , as well as the additional independent parameters AE^* or AE^{**} , are selected here, because it is well known that electron fluxes vary with altitude, electron energy, L -shell and geomagnetic activity. The magnetic latitude (MLAT) could have been used as an alternative to h since h and MLAT are directly related in a dipolar field but, as our goal is to provide model fluxes at given altitudes, directly using h is more practical in this case.

The variation of the omnidirectional electron flux with altitude is taken into account by adopting the functional form

$$J_{omni}(h) = B \cdot (\ln(h + 200))^C, \quad (7)$$

where J_{omni} is hereafter in units of $e/cm^2/s/MeV$, h in km, and the two variables B and C are supposed to depend on AE , L and E . Four reasons led us to adopt the functional form given in Equation (7):

- initial visual inspection has shown that $J_{omni}(h)$ increases slower at higher h ;
- Equation (5) implies that $J(h > h_0, \alpha_h = \pi/2)$ depends on a logarithmic function of h , $\ln(\sin \alpha_{eq}(\alpha_h = \pi/2) / \sin \alpha_{eq,LC}) \approx \ln(1 + 3h/2R_E)$;
- a simple functional form is usually preferable to avoid overfitting;
- the various other functional forms which have been tested, like power-law functions, provided less accurate fits to the data.

The dependence on geomagnetic activity (and its impact on flux variations with E and L) is taken into account by determining different values of B and C for each of the four levels AE_i^* and for each of the four levels AE_i^{**} defined above.

After numerous trials, we decided to keep B constant over each separate domain of geomagnetic activity. Next, it is important to choose an appropriate functional form for $C(L, E)$ on the basis of theoretical and observational knowledge. First, Equation (7) implies that $\ln(J_{omni}(h)/(J_{omni}(h_0)))$ is proportional to $C(L, E)$. Equation (5) shows that $\ln(J(h, \alpha_h = \pi/2)/J(h_0, \alpha_{h_0} = \pi/2))$ increases monotonically with $\ln(z_0)$, but slower than $\ln(z_0)$ at large z_0 , with $z_0 = 2\alpha_{eq,LC}(D_{\alpha\alpha}\tau_B)^{-1/2}$ and $D_{\alpha\alpha}$ the pitch-angle diffusion rate at $\alpha_{eq,LC}$. Therefore, $C(L, E)$ should increase monotonically with $\sim |\ln(D_{\alpha\alpha}\gamma/(\gamma^2 - 1)^{1/2})|/2 - 2\ln(L)$, although more slowly. The variation of $D_{\alpha\alpha}$ as a function of $L \in [1.5, 10]$ and $E \in [0.06, 1.5]$ MeV has been provided based on statistics of whistler-mode waves (Agapitov et al., 2018; Green et al., 2020; Q. Ma et al., 2016, 2017, 2022). It shows two different variations of $D_{\alpha\alpha}$ with E , increasing toward higher E at $L < 2.5-3$ and decreasing toward higher E at $L > 3.5$ (except within the plasma sheet above 0.5-1 MeV near 0 MLT, see Artemyev, Orlova, et al., 2013). Second, Equation (7) indicates that $\ln(J_{omni})$ is proportional to $C(L, E)$, and spacecraft observations have shown the presence of two L -shell domains with distinct energy spectra $J_{omni}(E)$, at $L \in [1.5, 3.5]$ where the flux rapidly decreases as E increases over 0.1–1.5 MeV, and the outer belt and near-Earth plasma sheet at $L \approx 4 - 7$ where the flux can decrease sensibly less rapidly toward higher E (Reeves et al., 2016). The above theoretical and observational facts therefore suggest using two slightly different forms of $C(L, E)$ in two separate L -shell domains: $L \in [1.5, 3.5]$ (domain 0) and $L \in [3.5, 10]$ (domain 1).

After various trials, the selected functional form of $C(L, E)$ is:

$$C = C_0 + C(L) + C(E, L) \quad (8)$$

where:

$$C(L) = C_1 \cdot L + C_2 \cdot L^2 + C_3 \cdot L^3 + \frac{C_4}{L} + \frac{C_5}{L^2}$$

and

$$C(E, L) = \begin{cases} C_6 \cdot \ln(E) + (3.5 - L) \cdot (C_8 \cdot \ln(E)^2 + C_9 \cdot \ln(E)^3) & \text{if } 1.5 < L < 3.5 \\ L \cdot (C_6 \sqrt{\ln(E)} + \frac{C_7}{\ln(E)} + C_8 \cdot \ln(E)^2 + C_9 \cdot \ln(E)) & \text{if } 3.5 < L < 10 \end{cases}$$

with E in keV and L the McIlwain magnetic shell parameter.

For each (AE_i^*, E, L) and (AE_i^{**}, E, L) , we use Powell's method (e.g., see Gill et al., 2020) on averaged $J_{omni}(h)$ values to determine the pair (B, C) minimizing the loss function $\text{MEF} \times EF_{90}$, where $\text{MEF} = \exp(M(|\ln(Q_j)|))$ is the Median Error Factor between model values and actual values of J_{omni} (where M denotes the median and Q_j values are ratios of model to actual values), and EF_{90} is the 90th percentile of the Error Factor, $EF = \exp(|\ln(Q_j)|)$. The MEF is equivalent to the Median Symmetric Accuracy introduced by Morley et al. (2018): it is particularly relevant for electron fluxes varying by orders of magnitude and robust to the presence of outliers and bad data (Morley et al., 2018; Zheng et al., 2019). Its meaning is simply that 50% of model fluxes are less than a factor of MEF from actual fluxes. The advantage of using the loss function $\text{MEF} \times EF_{90}$ is to simultaneously minimize MEF and EF_{90} , thereby ensuring that both 50% and 90% of model fluxes remain as close as possible to actual fluxes. This should provide a full distribution of model fluxes close to the full distribution of actual fluxes.

Accordingly, for each (AE_i^*, E, L) or (AE_i^{**}, E, L) corresponding to an averaged profile $J_{omni}(h)$ in altitude, we first use Powell's method to find an optimal value of B and C . Next, for each AE_i^* or AE_i^{**} at $L > 3.5$ and for all data at $L < 3.5$, we determine the coefficient B which allows to best approach these initial B values, using the classical least squares loss function. We then repeat, for each (AE_i^*, E, L) and (AE_i^{**}, E, L) , the Powell's optimization over h , using now the value of B corresponding to the relevant domain of AE_i^* or AE_i^{**} . This gives us new optimal values of C , which we use to get coefficients C_m in Equation (8) for each AE_i^* and AE_i^{**} level at $L > 3.5$ and for all AE at $L < 3.5$. The values of model coefficients B and C_m in each parameter domain are provided in the Appendix. Note that the model is trained over energies $E \in [60, 1500]$ keV at $L \in [1.5, 10]$ and should not be used outside of these limits. Finally, to obtain a smooth model of J_{omni} through the frontier at $L = 3.5$ between the two L domains, $J_{omni}(E, L)$ is interpolated between $L = 3.25$ and $L = 3.6$.

Figure 1 shows various examples of average omnidirectional differential electron flux $J_{omni}(h)$ profiles in altitude between $h = 150$ km and $h = 20,000$ km, either directly inferred from ELFIN A measurements (black crosses) or given by the model (blue solid line), at 100 keV and 500 keV and for different L -shells and geomagnetic activity levels. The uncertainty of average inferred fluxes is the sum of the uncertainty inherent to the method (estimated as a factor of ~ 1.5 at $L > 3.5$ in Section 2) and of the normalized standard error of the mean flux (usually of the order of 10% to 25%), evaluated based on the standard deviation and number of inferred fluxes. The corresponding error bars are provided (in red) in Figure 1. The difference between fluxes from the model and actual measured fluxes is usually less than a factor of ~ 1.5 , although it can sometimes increase to a factor of ~ 3 . One can also notice a rapid flux increase at low altitudes from 150 km to 2000 km, followed at $h > 2000$ km by a slower increase well fitted by the model.

Several metrics are used to assess the accuracy and the forecasting ability of the model. We calculate, for the training and the validation sets, MEF, EF_{90} and the Pearson correlation coefficient r between model values of J_{omni} and values inferred from ELFIN measurements. We do this each time for the whole set and for each domain of (AE_i^*, L) and (AE_i^{**}, L) separately. We also determine MEF and EF_{90} at three altitudes, $h = 150$ km, 2000 km, and the maximum altitude $h \leq 20,000$ km reached on the considered field line, for $E = 100$ keV, 500 keV, and 1.5 MeV, for each AE_i^* or AE_i^{**} level.

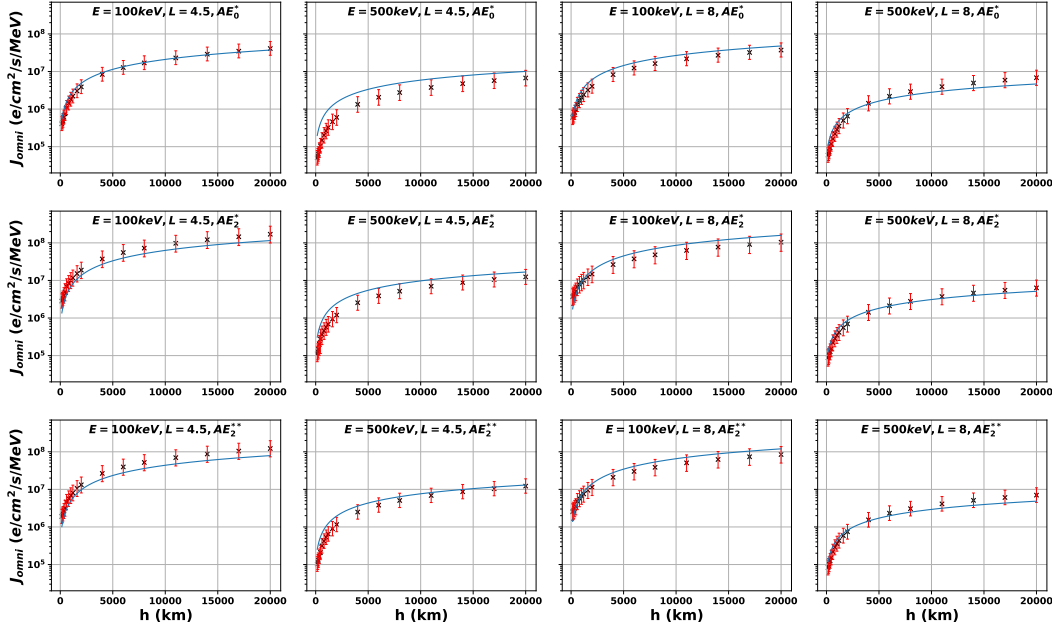


Figure 1: Average omnidirectional electron flux J_{omni} as a function of altitude h for different energies, L -shells, and geomagnetic activity levels, directly inferred from ELFIN A measurements (black crosses, with error bars in red) and given by the model (solid blue line).

AE level	L domain	r	MEF/EF_{90}	MEF/EF_{90} (150 km)	MEF/EF_{90} (2000 km)	MEF/EF_{90} (max. alt.)	MEF/EF_{90} (100 keV)	MEF/EF_{90} (500 keV)	MEF/EF_{90} (1.5 MeV)
all	0	0.95	1.8/3.7	2.8/5.6	1.5/2.3	1.5/3.6	2.2/4.3	1.9/3.5	2.2/6.0
AE_0^*	1	0.93	1.6/2.5	1.9/3.0	1.5/2.0	1.3/1.8	1.4/1.6	1.7/3.2	1.7/3.0
AE_1^*	1	0.92	1.3/2.2	1.5/2.6	1.2/1.7	1.4/2.5	1.2/1.5	1.4/2.5	1.8/3.1
AE_2^*	1	0.87	1.4/2.3	1.7/3.3	1.3/2.0	1.4/2.2	1.4/1.9	1.4/2.3	1.9/5.1
AE_3^*	1	0.76	1.4/2.8	1.8/3.3	1.3/2.7	1.5/2.7	1.4/2.2	1.6/3.1	1.8/4.6
AE_0^{**}	1	0.94	1.5/2.6	1.8/3.0	1.5/2.2	1.4/1.8	1.4/1.6	1.7/3.4	1.7/2.9
AE_1^{**}	1	0.85	1.3/2.6	1.6/3.1	1.3/2.2	1.4/2.9	1.3/1.7	1.6/3.1	1.8/4.2
AE_2^{**}	1	0.89	1.3/2.1	1.6/2.7	1.2/1.7	1.3/2.3	1.3/1.7	1.4/2.1	1.9/4.2
AE_3^{**}	1	0.85	1.4/2.5	1.6/3.3	1.3/2.1	1.4/2.4	1.3/1.9	1.3/2.9	1.7/3.6

Table 1: Accuracy metrics for the $J_{omni}(AE^*)$ and $J_{omni}(AE^{**})$ models

Table 1 shows the performance of the $J_{omni}(AE^*)$ and $J_{omni}(AE^{**})$ models on the training dataset (ELFIN A). The global accuracy metrics for both the AE^* and AE^{**} models are nearly identical, with a Pearson correlation coefficient $r = 0.86$, a median error factor $MEF \sim 1.4$, and a 90th percentile of the error factor $EF_{90} \sim 2.5$. These metrics are usually roughly similar for the two models at all altitudes and electron energies, demonstrating the good accuracy of these models throughout the parameter domains, thanks to a large sample size within each domain.

A comparison of the model with the validation dataset (ELFIN B) shows a similarly good agreement, with Pearson correlation coefficients of $r = 0.79$ and $r = 0.83$, global MEFs of 1.5 and 1.4, and global Error Factors EF_{90} of 3.1 and 3.0 for AE^* and AE^{**} models, respectively. Note that ELFIN A and B CubeSats often collect data from the same location (MLT sector) with a time lag of $\sim 0.05 - 30$ minutes between the two spacecraft, which is sufficient to measure significantly different precipitating or trapped electron fluxes (Zhang et al., 2023) and justifies using ELFIN B measurements as the validation set.

3.3 Omnidirectional Electron Flux Variations with MLT

Previous investigations of electron fluxes measured by Polar Operational Environmental Satellites (POES) in polar orbit at 850 km altitude found a non-negligible MLT asymmetry of trapped electron flux up to at least 300 keV at $L \sim 3-9$ (Allison et al., 2017; Meredith et al., 2016), increasing with geomagnetic activity (AE^*), with ≈ 2 times higher 100 – 300 keV electron flux in the dawn sector than in the dusk sector at $L = 3 - 7$ when $AE^* < 1000$ nT and the reverse at $L > 7$ during quiet periods (Allison et al., 2017). A dawn-dusk asymmetry of 200 – 350 keV electron flux by a factor of ≈ 2 has also been observed at $L = 1.3$ (Selesnick et al., 2016).

Such MLT variations are partly due the MLT asymmetry of substorm electron injections from the plasmasheet and to non-dipolar components in the actual geomagnetic field. Electron injections usually occur at 0-6 MLT. During their subsequent azimuthal drift toward dusk, injected electrons are efficiently precipitated by whistler-mode waves (at < 500 keV) or EMIC waves (at > 1 MeV) into the atmosphere, or lost through magnetopause shadowing at $L > 5$, leading to a lower electron flux in the dusk sector. A distortion of trapped electron drift shells by the solar wind-driven dawn-to-dusk convection electric field (Matsui et al., 2013) and ionospheric electric fields (Lejosne & Mozer, 2016; Califf et al., 2022) can also result in a dawn-dusk asymmetry in electron fluxes, a process which may operate down to $L = 1.3$ (Selesnick et al., 2016).

As in the above-discussed previous works, the time-averaged $J_{omni}(h, MLT)$ measured (at $h = h_0$) or inferred from ELFIN data in each MLT sector exhibits a non-negligible MLT modulation at all E and L , usually by a factor of ≈ 2 . To approximately take this MLT modulation into account, we minimize $J_{omni}(MLT)/\langle J_{omni} \rangle - M(MLT, K)$, where $M(MLT, K) = 1 + 0.33 \sin(2\pi MLT/24 + K)$ and the average is performed over MLT, giving us a K value for each (L, AE_i^*) or (L, AE_i^{**}) domain, provided in the Appendix. Multiplying the MLT-averaged $J_{omni}(h)$ from the ELFIN-based model by the function $M(MLT, K)$ allows to roughly incorporate MLT modulations. The resulting new version, with MLT modulation, of the ELFIN-based J_{omni} model is however in slightly less good agreement with MLT-averaged J_{omni} values inferred from ELFIN data than the baseline MLT-averaged model. Figure 2 shows 100 keV and 300 keV electron fluxes of the model with MLT modulation at $L = 5$ and $h = 450$ km (blue curve), compared with actual electron fluxes measured by ELFIN in different MLT sectors (red circles).

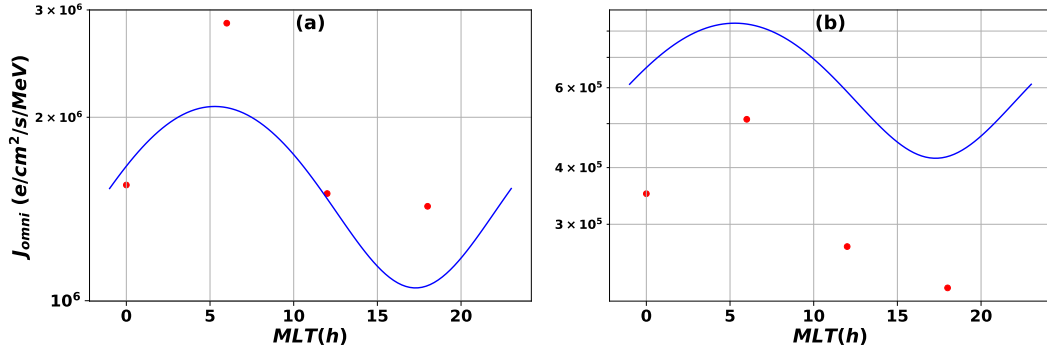


Figure 2: (a) Model omnidirectional electron flux with included MLT modulation, $J_{omni}(MLT) = J_{omni} \times M(MLT, K)$ at 100 keV, $L = 5$, and $h = 450$ km (in blue), as a function of MLT following periods of quiet geomagnetic conditions (AE_1^*), with corresponding fluxes $J_{omni}(MLT)$ directly inferred from ELFIN A measurements (in red). (b) Same as (a) for 300 keV electrons.

4 Analysis of Model Results

4.1 Electron Flux Variations with Geomagnetic Activity

Figures 3 and 4 show maps of the model omnidirectional electron flux $J_{omni}(E, L)$ for $L = 1.5 - 10$ at low and high altitudes, $h = h_0 = 450$ km and $h = \min(20,000 \text{ km}, (L-1) \times 6371 \text{ km})$, respectively, following periods of quiet and disturbed geomagnetic conditions, defined by AE_0^* and AE_2^* levels (top row) or AE_0^{**} and AE_2^{**} levels (bottom row). The selected altitudes $h \leq h_{max}$ in Figure 4 correspond to the magnetic equator from $L = 1.5$ to $L = 4.15$. Figures 3 and 4 demonstrate that the model describes well the structure of electron fluxes in the inner magnetosphere from $L = 1.5$ up to $L = 10$, with a first flux peak in the inner radiation belt at $L = 1.5 - 2$, low fluxes in the slot region at $L \simeq 3 - 3.5$ due to hiss wave-driven electron loss (Lyons & Thorne, 1973; Mourenas et al., 2017), high 0.3 – 1.5 MeV electron fluxes in the outer radiation belt at $L \simeq 4 - 7$, and the plasma sheet at $L > 7$. Note that the present model provides only time-averaged fluxes at $L < 3.25$, with exactly the same fluxes in left and right columns of Figures 3 and 4. This is justified by the much weaker variation of time-averaged electron fluxes with geomagnetic activity at $L \lesssim 3$ than at $L > 3.5$ (Mourenas et al., 2017; Reeves et al., 2016).

The average omnidirectional flux is rapidly decreasing from 60 keV to 1.5 MeV at all L -shells, but less steeply within the outer radiation belt (at $L \simeq 4 - 7$) than in the plasma sheet (at $L > 7$). This is likely due to two physical processes: an adiabatic acceleration of electrons as they travel from $L \sim 10$ to $L \sim 4$ toward a stronger geomagnetic field (partly through inward radial diffusion by ULF waves, see Ozeke et al., 2014; Hudson et al., 2021), and an efficient local energization of $\sim 100 - 500$ keV electrons by chorus waves in low plasma density regions of the outer radiation belt at $L = 3.5 - 7$ (Agapitov et al., 2019; Horne et al., 2005; Summers et al., 1998; Thorne et al., 2013).

In the outer radiation belt, the radial (L) position of the maximum average omnidirectional 100 – 500 keV electron flux comes closer to the Earth, down to $L \simeq 4 - 4.5$, after periods of high geomagnetic activity (e.g., compare black contours of flux for AE_0^{**} and AE_2^{**} levels in Figure 4). The radial position of this maximum of $J_{omni}(L)$ after active periods is consistent with the position of the peak of chorus wave-driven electron energization inferred from statistical wave and plasma measurements, which similarly moves to lower L after disturbed periods (Agapitov et al., 2019). Equatorial mea-

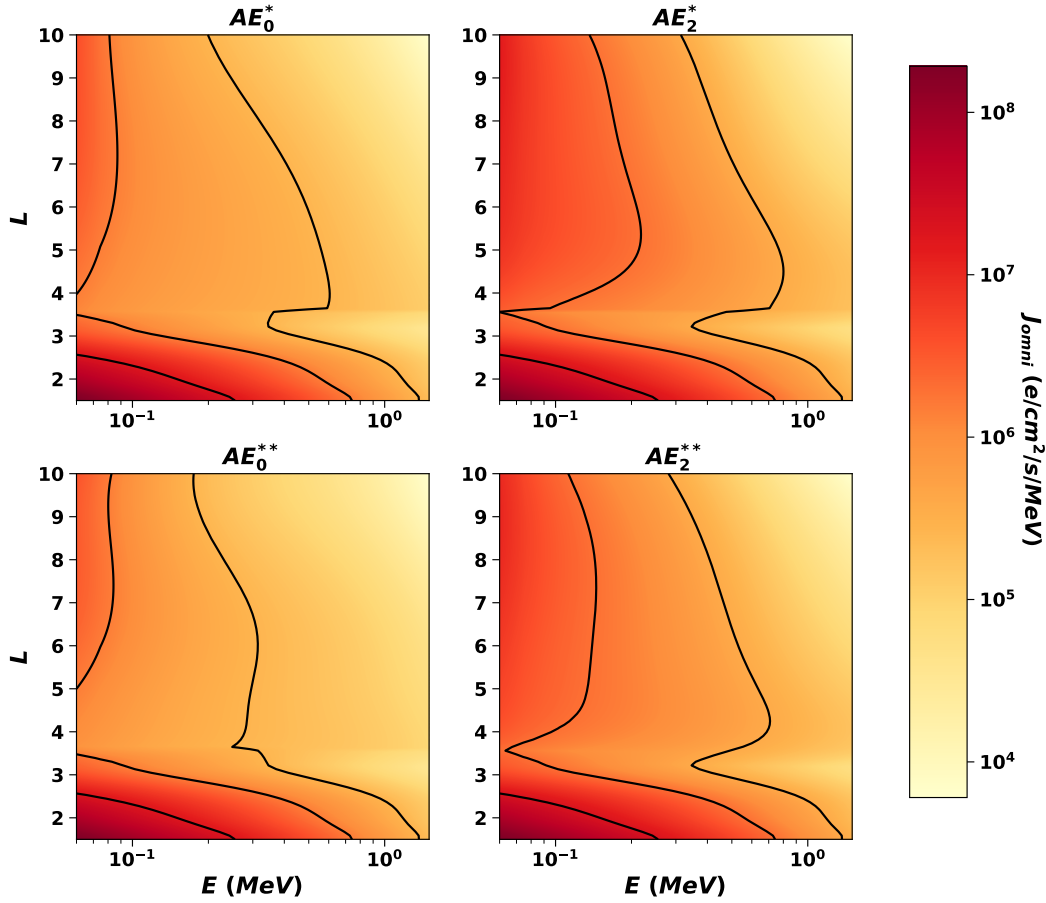


Figure 3: Model average omnidirectional electron flux $J_{omni}(E, L, h)$ as a function of energy E and L -shell at the altitude $h = h_0 = 450$ km of ELFIN A measurements, following periods of quiet (left) and disturbed (right) geomagnetic conditions, corresponding to AE_0^* and AE_2^* levels (top row) or AE_0^{**} and AE_2^{**} levels (bottom row). Black contours show $1/10$, $1/100$, and $1/500$ of the maximum flux in the color scale on the right-hand-side.

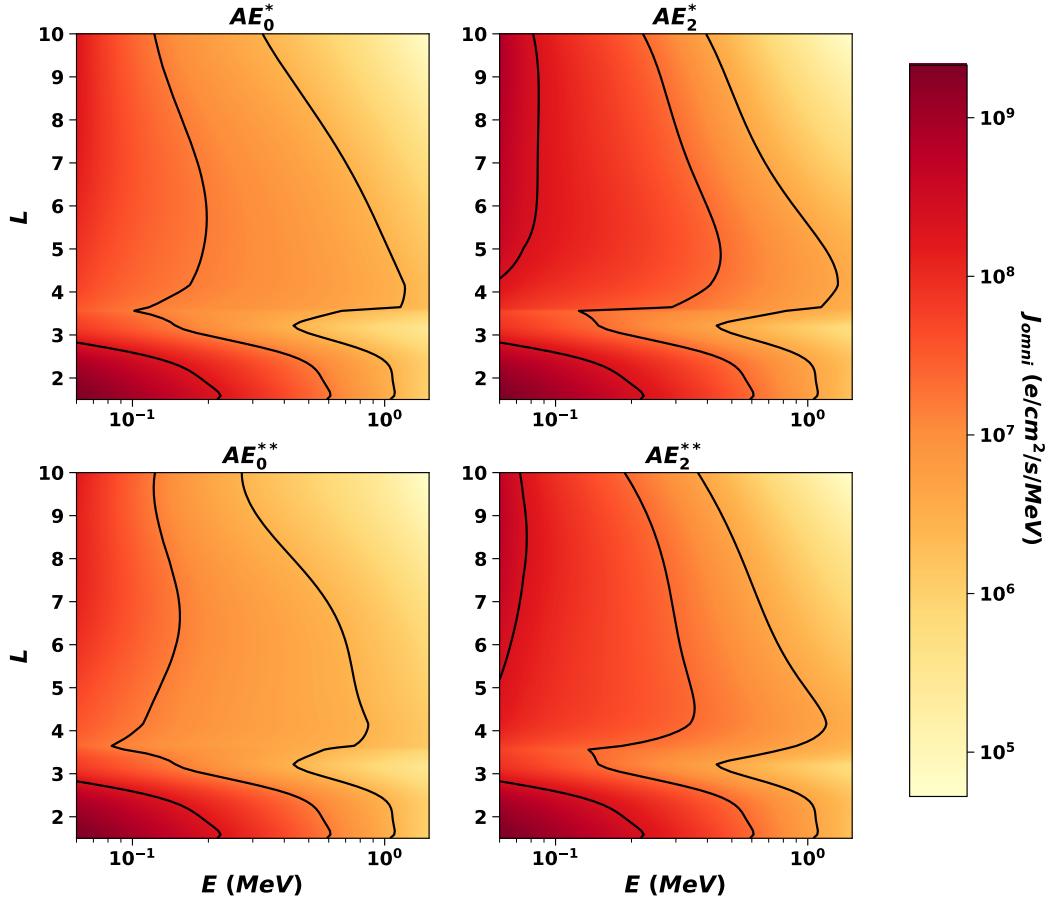


Figure 4: Model average omnidirectional electron flux $J_{omni}(E, L, h)$ as a function of energy E and L -shell at $h = \min(20,000 \text{ km}, (L - 1) \times 6371 \text{ km})$, for quiet (left) and disturbed (right) geomagnetic conditions, corresponding to AE_0^* and AE_2^* levels (top row) or AE_0^{**} and AE_2^{**} levels (bottom row). Black contours show 1/10, 1/100, and 1/500 of the maximum flux in the color scale on the right-hand-side.

surements from the Van Allen Probes likewise show a maximum of omnidirectional 100–500 keV electron flux at $L > 5–6$ during quiet periods, moving to $L \simeq 4–4.5$ during geomagnetic storms (Reeves et al., 2016).

Following periods of high impulsive or time-integrated geomagnetic activity (corresponding to AE_2^* or AE_2^{**} levels, respectively), injections from the outer plasma sheet become more intense and both chorus and ULF wave power increase, leading to higher J_{omni} at $L > 3.5$ than after quiet periods (corresponding to AE_0^* or AE_0^{**} levels), at all energies. In the outer radiation belt, this increase of J_{omni} is stronger at $L \simeq 4–5$ in Figure 4. The electron flux above 200 keV is initially low during quiet times at $L = 4–10$, but it is lower for AE_0^{**} than for AE_0^* , because electron flux measurements corresponding to AE_0^* (that is, with a mean $AE < 100$ nT during the past 4 hours) are sometimes associated to significant time-integrated geomagnetic activity over the past 72 hours (AE_1^{**} or AE_2^{**} levels) that have already increased electron fluxes. Indeed, electron energization at $L \simeq 4–5$ is often a cumulative process, requiring many hours of elevated geomagnetic activity (Hua et al., 2022; Mourenas et al., 2019; Mourenas, Agapitov, et al., 2022; Thorne et al., 2013). Figure 4 shows that whatever the geomagnetic activity during the preceding 4 hours (AE^*), the level of J_{omni} will also partly depend on the level of time-integrated geomagnetic activity over the preceding 3 days (AE^{**}).

Therefore, Figure 4 demonstrates the important role of time-integrated geomagnetic activity (AE^{**}) in controlling the average omnidirectional electron flux over a very wide parameter range, from ~ 60 keV to 1.5 MeV and from $L = 3.5$ to $L = 10$. This suggests that the build-up of energetic electron fluxes often takes place over many consecutive hours in the near-Earth plasma sheet, even before reaching the outer radiation belt, probably through progressive convection and betatron acceleration within dipolarizing flux bundles at $L \sim 9–15$ (e.g., see Gabrielse et al., 2017, and references therein), as well as through electron inward radial diffusion and chorus wave-driven energization closer to the Earth (Mourenas, Agapitov, et al., 2022; Ozeke et al., 2014; Simms et al., 2021; Thorne et al., 2013). Nevertheless, the significant increase of electron fluxes with AE^* in Figure 4 indicates a strong concomitant influence of impulsive events in shaping energetic and relativistic electron fluxes at $L = 3.5–10$.

4.2 Comparisons with Van Allen Probes, THEMIS, and POES Data

The average J_{omni} from the present model (blue line) is compared in Figure 5 to the corresponding average flux inferred from ELFİN data (red pluses with error bars) and to the average omnidirectional electron flux measured by the Magnetic Electron Ion Spectrometer (MagEIS) aboard the Van Allen Probes (Blake et al., 2013; Claudepierre et al., 2021) in 2017–2018 less than 10° from the magnetic equator (black crosses). We use MagEIS data from 2017–2018, because this period, like the 2020–2022 period of ELFİN measurements, took place within 3 years of the solar cycle minimum of December 2019, suggesting roughly similar space weather properties during these two periods. Electron fluxes are displayed at $L \approx 4.5$ and $h = 22,000$ km in Figures 5(a)–5(d) for geomagnetic activity levels AE_0^* , AE_2^* , AE_0^{**} , and AE_2^{**} . Time-averaged fluxes (averaged over all AE levels) from the model at $L \approx 3.0$ and $h = 12,600$ km and at $L \approx 1.5$ and $h = 3,150$ km are also displayed in Figures 5(e) and 5(f), respectively, with corresponding average fluxes inferred from ELFİN data and measured by the Van Allen Probes in 2017–2018. Thanks to numerous data, the typical standard normalized error on average fluxes from the Van Allen Probes is only 4.5% (it is always less than 8.5%).

The adopted altitudes $h(L)$ for model and inferred fluxes in Figure 5 correspond to the magnetic equator, as required for comparisons with the bulk of the Van Allen Probes measurements. As average fluxes are inferred from ELFİN data at the same 18 pre-determined altitudes h_n for all L , a slight logarithmic extrapolation is performed to obtain values at $h(L)$ displayed in Figure 5, using $\ln(J_{omni}(h(L))/J_{omni}(h_n))/\ln(J_{omni}(h_{n-1})/J_{omni}(h_n)) =$

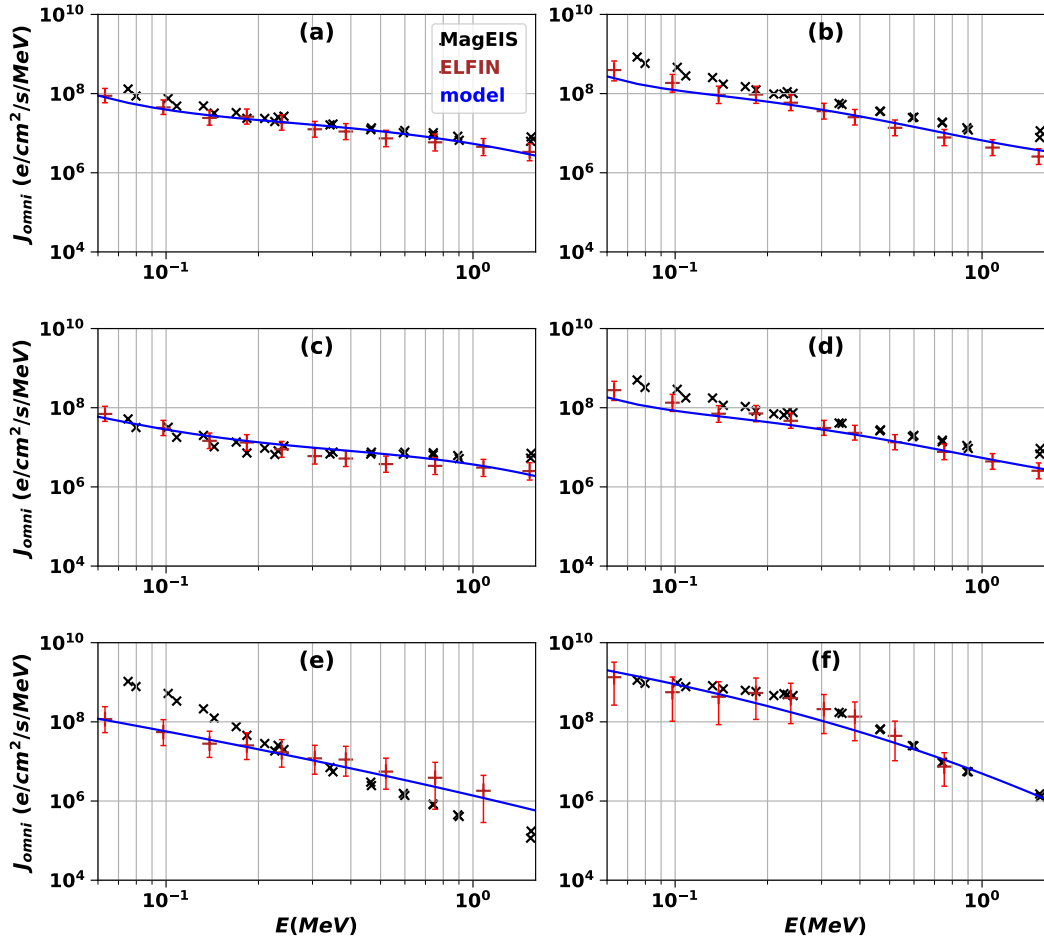


Figure 5: (a) Model average $J_{omni}(E)$ at $L \approx 4.5$ and $h = 22,000$ km for the low geomagnetic activity level AE_0^* (blue curve), corresponding average flux inferred from ELFIN data (red pluses with error bars), and corresponding average omnidirectional electron flux from MagEIS onboard the Van Allen Probes near the magnetic equator in 2017-2018 (black crosses). (b,c,d) Same as (a) for geomagnetic activity levels AE_2^* , AE_0^{**} , and AE_2^{**} , respectively. (e) Same as (a) at $L \approx 3.0$ and $h = 12,600$ km but averaged over all AE domains. (f) Same as (e) at $L \approx 1.5$ and $h = 3,150$ km.

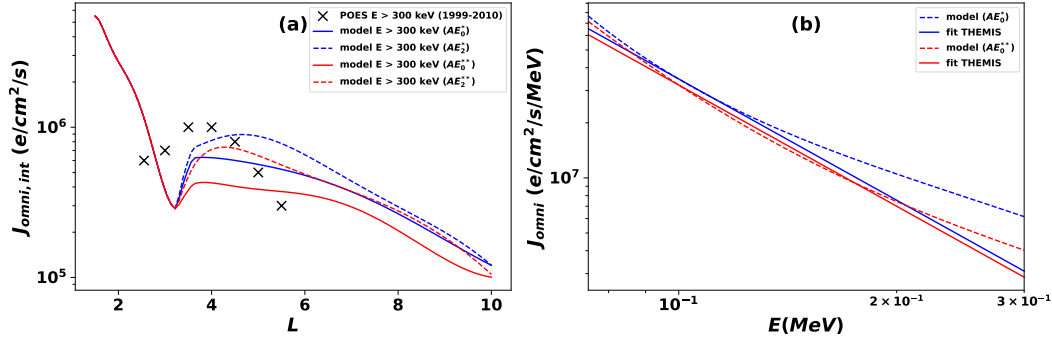


Figure 6: (a) Average integral omnidirectional electron flux from the present model at $E > 300$ keV for $h \simeq 850$ km and geomagnetic activity levels AE_0^* and AE_2^* (blue solid and dashed curves, respectively), as well as AE_0^{**} and AE_2^{**} (red solid and dashed curves, respectively) as a function L , with corresponding average fluxes from POES in 1999-2010 (black crosses). (b) Model $J_{omni}(E)$ at $L = 9$ and $h = 20,000$ km for geomagnetic activity levels AE_0^* and AE_0^{**} (dashed blue and red curves, respectively), and normalized power-law fits $J_{omni}(E)/J_{omni}(100 \text{ keV}) \approx (100 \text{ keV}/E)^\alpha$ with $\alpha = 2.2$ (solid blue and red lines) corresponding to typical omnidirectional 75 – 300 keV electron flux energy spectra measured by THEMIS spacecraft at $L \approx 9$ around the magnetic equator in 2008-2020.

$\ln(h(L)/h_n)/\ln(h_{n-1}/h_n)$, where h_n and h_{n-1} are the two closest altitudes below $h(L)$ where inferred fluxes are available. Note, however, that $h(L)$ is slightly higher than $h_{max}(L)$ given by Equation (6) at $L = 4.5$, which may lead to larger discrepancies between model fluxes and actual fluxes than at $h < h_{max}$ (see Section 2). In addition, the present J_{omni} model has been fitted to fluxes inferred from ELFIN data only at $h \leq h_n \leq 20,000$ km. But the slow increase with h of both modelled and inferred $J_{omni}(h)$ at $h > 4,000$ km (e.g., see Figure 1) suggests that the model should remain approximately valid up to $h = 22,000$ km at $L = 4.5$.

Figure 5 shows that the average electron flux of the model usually remains close to the average flux measured in 2017-2018 by the Van Allen Probes near the magnetic equator, from $L = 1.5$ to $L = 4.5$ over the whole parameter range. Global metrics for the AE^* and AE^{**} models compared to Van Allen Probes fluxes are median error factors $MEF = 2.1$ for both geomagnetic activity indicators, with 90th percentiles of the error factor $EF_{90} = 6.0$ and $EF_{90} = 6.9$, and Pearson correlation coefficient $r = 0.60$ for both. Notably, the increase of electron fluxes from the Van Allen Probes with geomagnetic activity at 100 – 900 keV is well reproduced by the model at $L = 4.5$. The average electron flux of the model decreases faster at $L = 1.5 - 3$ than at $L = 4.5$ from 100 keV to 1.5 MeV, and it is much lower in the slot region at $L = 3$ than in both the inner radiation belt at $L = 1.5$ and the outer radiation belt at $L = 4.5$ above 100 keV, in agreement with observations from the Van Allen Probes. The slot region is produced by hiss wave-driven electron precipitation into the atmosphere (Lyons & Thorne, 1973; Q. Ma et al., 2016; Mourenas et al., 2017).

The comparisons in Figure 5 therefore provide a validation of the present method for inferring omnidirectional electron fluxes at all altitudes along a geomagnetic field line based on low-altitude ELFIN data of trapped, precipitating, and backscattered electron fluxes. The largest discrepancy between model and Van Allen Probes fluxes occurs at 70 – 150 keV and $L = 3$, where average fluxes from the model are $\approx 4 - 8$ times lower than Van Allen Probes fluxes. This could partly reflect actual differences between electron fluxes in 2020-2022 and 2017-2018. But this discrepancy is probably also due to pe-

cularities of wave-driven electron pitch-angle diffusion rates at $L \approx 3$, which sometimes exhibit a bottleneck (a deep trough) at moderately high pitch-angles and low energy, leading to much larger fluxes than in the present model above $\alpha_{eq} = 60^\circ$ (see Section 2).

Figure 6(a) further shows the average energy-integrated omnidirectional electron flux at $E > 300$ keV from the present ELFIN-based model at $h \simeq 850$ km, for geomagnetic activity levels AE_0^* and AE_2^* (blue solid and dashed curves, respectively) as well as AE_0^{**} and AE_2^{**} (red solid and dashed curves, respectively), and the average > 300 keV electron fluxes measured by Polar Operational Environmental Satellites (POES) in polar orbit at ~ 850 km altitude (Yando et al., 2011). Only average POES fluxes measured in 1999–2010 (black crosses) at adiabatically invariant shells $L^* \leq 5.5$ (Sicard et al., 2018) are displayed, because deviations of L^* from L usually remain moderate in this domain, allowing us to assume that $L \approx L^*$ to first order. Figure 6(a) shows a reasonable agreement between time-averaged fluxes from POES and from the present model at $L \approx 2.5 - 5.5$, especially taking into account that they correspond to different time intervals of measurements, belonging to different solar cycles.

Finally, Figure 6(b) shows that the model energy spectra $J_{omni}(E)$ at $L = 9$ and $h = 20,000$ km for low geomagnetic activity levels AE_0^* (dashed blue curve) and AE_0^{**} (dashed red curve) are in good agreement with the typical (median) energy spectrum shape $J_{omni}(E)/J_{omni}(100 \text{ keV}) \approx (100 \text{ keV}/E)^\alpha$ with $\alpha = 2.2 \pm 0.5$ (solid blue and red lines) of omnidirectional 75–300 keV electron fluxes measured by Time History of Events and Macroscale Interactions during Substorms (THEMIS) spacecraft (Angelopoulos et al., 2008) at $L \approx 9 \pm 2$ around the equator (corresponding to fluxes higher than model fluxes) in the near-Earth plasma sheet in 2008–2020 (Gao et al., 2023). At $L \approx 9$, an altitude $h = 20,000$ km is far from the magnetic equator, but while the absolute level of J_{omni} should decrease as latitude increases along closed magnetic field lines, one expects a roughly similar variation of $J_{omni}(E)$ with energy $E \in [75, 300]$ keV at different altitudes $h \gtrsim 20,000$ km when these electrons are sufficiently strongly scattered in pitch-angle to reach $h = 450$ km in large numbers (Gao et al., 2022; Mourenas et al., 2024; Shane et al., 2023).

4.3 Corresponding Sinusoidal Equatorial Pitch-Angle Distributions

The pitch-angle distribution of electrons in the Earth’s radiation belts has been examined in many past studies, often using simple fits of the form $J(\alpha_{eq}) = \sin^n \alpha_{eq}$, with n the pitch-angle index (Gannon et al., 2007; R. Shi et al., 2016; Zhao et al., 2014). Therefore, it is interesting to compare the new ELFIN-based model, based on low-altitude measurements with good resolution at low equatorial pitch-angles, with these past results derived from spacecraft measurements at high altitude around the magnetic equator with a low resolution at low equatorial pitch-angles but a good resolution at high equatorial pitch-angles. Figure 7 shows the pitch-angle index n calculated using Equations (4) and (5) under the assumption that $J(\alpha_{eq}) = \sin^n \alpha_{eq}$ based on the average precipitating to trapped flux ratio J_{prec}/J_{trap} measured at low altitude by ELFIN, for 0.1, 0.5, and 1.5 MeV at $L = 1.5 - 10$, for quiet (AE_0^*) and active (AE_2^*) geomagnetic conditions. Figure 7(a) shows a first estimate of n calculated between $\alpha_{eq} = 10^\circ$ and $\alpha_{eq} = 90^\circ$. Figure 7(b) shows a second estimate of n calculated between $\alpha_{eq} = 1.1 \times \alpha_{eq,LC}$ and $\alpha_{eq} = 90^\circ$. These two estimates of n are expected to be roughly similar to estimates obtained in previous works by fitting the measured equatorial pitch-angle electron distribution at $\alpha_{eq} > 5^\circ - 15^\circ$. The second n estimate may also allow inferring $J(\alpha_{eq} = 90^\circ)$ from $J(\alpha_{h_0} \simeq 90^\circ)$ measured by ELFIN. A best fit $n = 0.59 + 0.22 \times (10/L)^{1.09}$ (solid green curve) to this second estimate for AE_0^* periods is shown in Figure 7(b).

For 0.1 MeV, 0.5 MeV, and 1.5 MeV electrons, Figure 7 shows that the pitch-angle index n inferred from ELFIN low-altitude measurements decreases as L increases, from $n \simeq 1.75 - 2.5$ at $L = 1.5 - 2.5$ to $n \simeq 0.35 - 1.25$ at $L = 4 - 10$, with a slightly lower n

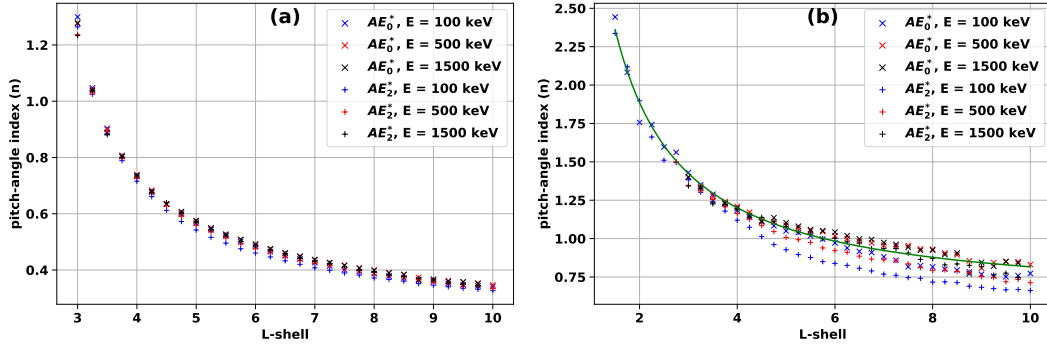


Figure 7: (a) Pitch-angle index n estimated between $\alpha_{eq} = 10^\circ$ and $\alpha_{eq} = 90^\circ$ based on the average precipitating to trapped flux ratio J_{prec}/J_{trap} measured by ELFIN, as a function of L for 100 keV (blue), 500 keV (red), and 1.5 MeV (black) electrons, following quiet (AE_0^*) and disturbed (AE_2^*) periods (crosses and pluses, respectively). (b) Same as (a) but showing n estimated between $\alpha_{eq} = 1.1 \times \alpha_{eq,LC}$ and $\alpha_{eq} = 90^\circ$, with a best fit $n = 0.59 + 0.22 \times (10/L)^{1.09}$ to AE_0^* model values (solid green curve).

at lower energy or after disturbed periods (AE_2^*). This decrease of n toward higher L , lower E , or after stronger geomagnetic activity, is due to a stronger wave-driven pitch-angle diffusion that results in a flatter pitch-angle distribution and a higher J_{prec}/J_{trap} (Agapitov et al., 2018; Kennel & Petschek, 1966; Mourenas et al., 2024). These results are in good agreement with previous works based on near-equatorial electron fluxes measured by the Van Allen Probes, which obtained $n \approx 2 - 4$ at $L = 1.5 - 2.5$ and $n \approx 0.5 - 1.2$ at $L = 3.5 - 6$ for 0.1 - 1 MeV electrons and a slightly lower n at lower energy (Allison et al., 2018; R. Shi et al., 2016; Zhao et al., 2014), as well as a slightly lower n after disturbed periods at $L = 4 - 5$ (Olifer et al., 2022). However, these previous works also found high indices $n \geq 5$ for 100–350 keV at $L \approx 3$, contrary to the present results. The good agreement between average fluxes J_{omni} from the ELFIN-based model and average fluxes from Van Allen Probes 2017-2018 measurements near the magnetic equator at $L = 3$ for 200–350 keV in Figure 5(e) suggests that this discrepancy is probably due to a dominant contribution, in time-averaged fluxes, from high fluxes characterized by $n \approx 1.5$ at $L = 3$, while higher indices $n > 5$ correspond to more frequent but much lower fluxes (R. Shi et al., 2016).

5 Conclusions

In the present work, energy- and pitch-angle-resolved precipitating, trapped, and backscattered electron fluxes measured at 450 km altitude by ELFIN CubeSats in 2020-2022 have been used to infer omnidirectional fluxes of 60 keV to 1.5 MeV electrons at $L = 1.5 - 10$, from 150 km up to 20,000 km altitude, using adiabatic transport theory and quasi-linear diffusion theory. The inferred fluxes have been fitted by analytical formulas, using stepwise multivariate optimization. The resulting self-consistent model of omnidirectional electron flux J_{omni} , inferred from measurements from only one spacecraft at a time in LEO, is free from potential conjunction or intercalibration problems arising when combining measurements from different spacecraft. The present modelled electron fluxes are intrinsically coherent at all altitudes along each geomagnetic field line. Such modelled electron fluxes are provided as a function of electron energy E , L -shell, altitude, and of two different indices, AE^* and AE^{**} , of geomagnetic activity over the preceding 4 hours and over the previous 72 hours, respectively.

The obtained model of omnidirectional electron flux has been validated by comparisons with Van Allen Probes measurements near the magnetic equator at high altitudes and $L \simeq 1.5 - 4.5$ in 2017-2018, THEMIS measurements at $L \approx 9$ around the equator in 2008-2020, and POES measurements at 850 km altitude and $L \simeq 2.5 - 5.5$ in 1999-2010. A version of the model includes MLT modulations similar to previous observations. The equatorial pitch-angle electron distributions corresponding to the present ELFIN-based model are also in rough agreement with previous works. Such comparisons show that the present method for inferring omnidirectional electron fluxes at all altitudes along a given magnetic field line based only on pitch-angle and energy resolved electron flux measurements from one low-altitude spacecraft is essentially valid from $L \sim 1.5$ to 10 above 60 keV, at least up to an altitude of $\approx 20,000$ km. This study therefore suggests that a fleet of low-cost CubeSats similar to ELFIN could be used to monitor the radiation belts from low Earth orbit via the present method (Millan et al., 2024).

The obtained model of omnidirectional electron flux allowed us to show that both impulsive geomagnetic activity (AE^*) and time-integrated geomagnetic activity (AE^{**}) are partly controlling the average level of 60–1500 keV electron fluxes over a very wide L -shell domain, extending from $L = 3.5$ to $L = 10$. This new analytical model can be used for various tasks: (a) to obtain event-specific boundary conditions for radiation belt numerical models (e.g., see Tu et al., 2014), (b) to assess the main physical processes at work through an examination of the latitudinal distribution of electron fluxes along field lines, (c) to disentangle the effects of rapid processes (such as direct electron injections) from the effects of slower cumulative processes (such as electron inward radial diffusion and wave-driven diffusive energization) by taking advantage of the functional dependence of modelled fluxes on two different geomagnetic activity indices (corresponding to brief and prolonged processes, respectively), and (d) to estimate or forecast the radiation dose along a given orbit and the related internal or surface charging hazards for satellites. Since the modelled J_{omni} is provided in two separate versions, $J_{omni}(AE^*)$ and $J_{omni}(AE^{**})$, better estimates or forecasts of the omnidirectional electron flux may also be obtained by using an average of $J_{omni}(AE^*)$ and $J_{omni}(AE^{**})$, based on three-day sequences of measured or predicted AE values.

Acknowledgments

A.V.A., X.J.Z., and V.A. acknowledge support by NASA awards 80NSSC20K1270, 80NSSC23K0403, 80NSSC24K0558, NAS5-02099, and NSF grants AGS-1242918, AGS-2019950, and AGS-2021749. We are grateful to NASA’s CubeSat Launch Initiative for ELFIN’s successful launch. We acknowledge early support of the ELFIN project by the AFOSR, under its University Nanosat Program; by the UNP-8 project, contract FA9453-12-D-0285; and by the California Space Grant program. We sincerely acknowledge the critical contributions of the numerous volunteer ELFIN team student members.

Open Research

Electron fluxes measured by ELFIN are available in CDF format (ELFIN, 2024). Van Allen Probes MagEIS electron flux data (REL03 L2) is available from the New Mexico Consortium (VAN ALLEN PROBES, 2024). The SME index (Gjerloev, 2012) is available at the SuperMAG data archive (SUPERMAG, 2024). Data access and processing was done using SPEDAS V3.1, see Angelopoulos et al. (2019).

Appendix A Model coefficients without/with MLT modulation

The coefficients B and C_m in Equations (7) and (8) for the MLT-averaged model are provided in each parameter domain in Table A1 for both AE^* and AE^{**} models. The additional coefficients K , allowing to incorporate a MLT modulation in the MLT-averaged model (see Section 3.3), are provided in Table A2 in each parameter domain.

AE level	L domain	B	C_0	C_1	C_2	C_3	C_4	C_5	C_6	C_7	C_8	C_9
all	0	0.705	-590.88	282.36	-65.015	5.830	634.4	-261.5	-0.603	N/A	0.0251	-0.00523
AE_0^*	1	0.372	-17.68	-11.05	-0.382	0.0119	70.1	-77.6	6.413	18.9	-0.0502	-0.254
AE_1^*	1	0.391	3.79	-88.83	-0.145	0.00519	4.34	-3.72	64.160	61.9	0.238	-14.34
AE_2^*	1	0.462	84.94	-209.59	1.009	-0.0314	-218.7	231.5	147.833	122.0	0.670	-34.96
AE_3^*	1	0.436	-6.86	-153.65	0.0110	-0.00303	75.6	-130.1	111.192	103.5	0.424	-25.04
AE_0^{**}	1	0.304	-87.24	111.16	-1.390	0.0443	262.4	-283.5	-75.879	-49.3	-0.421	19.10
AE_1^{**}	1	0.413	33.36	-196.69	0.417	-0.0143	-59.1	40.6	141.199	123.6	0.599	-32.70
AE_2^{**}	1	0.451	-35.33	-136.60	-0.326	0.00614	158.2	-221.3	105.545	90.3	0.458	-24.66
AE_3^{**}	1	0.528	113.16	-149.56	0.935	-0.0225	-348.4	428.2	96.831	90.7	0.368	-21.78

Table A1: B and C coefficients associated to AE^* or AE^{**}

AE level	L domain	K_{AE^*}	$K_{AE^{**}}$
all	0	2.68	2.68
AE_0^* or AE_0^{**}	1	1.83	1.64
AE_1^* or AE_1^{**}	1	0.19	5.80
AE_2^* or AE_2^{**}	1	0.16	6.11
AE_3^* or AE_3^{**}	1	5.52	0.57

Table A2: Coefficients K for the MLT correction to models associated to AE^* and AE^{**}

References

- Agapitov, O. V., Mourenas, D., Artemyev, A., Hospodarsky, G., & Bonnell, J. W. (2019, June). Time Scales for Electron Quasi-linear Diffusion by Lower-Band Chorus Waves: The Effects of ω_{pe}/Ω_{ce} Dependence on Geomagnetic Activity. *Geophys. Res. Lett.*, *46*(12), 6178-6187. doi: 10.1029/2019GL083446
- Agapitov, O. V., Mourenas, D., Artemyev, A. V., Mozer, F. S., Hospodarsky, G., Bonnell, J., & Krasnoselskikh, V. (2018, January). Synthetic Empirical Chorus Wave Model From Combined Van Allen Probes and Cluster Statistics. *Journal of Geophysical Research (Space Physics)*, *123*(1), 297-314. doi: 10.1002/2017JA024843
- Allison, H. J., Horne, R. B., Glauert, S. A., & Del Zanna, G. (2017). The magnetic local time distribution of energetic electrons in the radiation belt region. *J. Geophys. Res. (Space Physics)*, *122*(8), 8108-8123. doi: 10.1002/2017JA024084
- Allison, H. J., Horne, R. B., Glauert, S. A., & Del Zanna, G. (2018, November). Determination of the Equatorial Electron Differential Flux From Observations at Low Earth Orbit. *Journal of Geophysical Research (Space Physics)*, *123*(11), 9574-9596. doi: 10.1029/2018JA025786
- Angelopoulos, V., Cruce, P., Drozdov, A., Grimes, E. W., Hatzigeorgiu, N., King, D. A., ... Schroeder, P. (2019, January). The Space Physics Environment Data Analysis System (SPEDAS). *Space Sci. Rev.*, *215*, 9. doi: 10.1007/s11214-018-0576-4
- Angelopoulos, V., Sibeck, D., Carlson, C. W., McFadden, J. P., Larson, D., Lin, R. P., ... Sigwarth, J. (2008, December). First Results from the THEMIS Mission. *Space Sci. Rev.*, *141*, 453-476. doi: 10.1007/s11214-008-9378-4
- Angelopoulos, V., Tsai, E., Bingley, L., Shaffer, C., Turner, D. L., Runov, A., ... Zhang, G. Y. (2020, July). The ELFIN Mission. *Space Sci. Rev.*, *216*(5), 103. doi: 10.1007/s11214-020-00721-7
- Angelopoulos, V., Zhang, X. J., Artemyev, A. V., Mourenas, D., Tsai, E., Wilkins, C., ... Zarifian, A. (2023, August). Energetic Electron Precipitation Driven by Electromagnetic Ion Cyclotron Waves from ELFIN's Low Altitude Perspective. *Space Sci. Rev.*, *219*(5), 37. doi: 10.1007/s11214-023-00984-w
- Artemyev, A. V., Mourenas, D., Agapitov, O. V., & Krasnoselskikh, V. V. (2013, April). Parametric validations of analytical lifetime estimates for radiation belt electron diffusion by whistler waves. *Annales Geophysicae*, *31*, 599-624. doi: 10.5194/angeo-31-599-2013
- Artemyev, A. V., Mourenas, D., Zhang, X. J., & Vainchtein, D. (2022, September). On the Incorporation of Nonlinear Resonant Wave-Particle Interactions Into Radiation Belt Models. *Journal of Geophysical Research (Space Physics)*, *127*(9), e30853. doi: 10.1029/2022JA030853
- Artemyev, A. V., Orlova, K. G., Mourenas, D., Agapitov, O. V., & Krasnoselskikh, V. V. (2013, September). Electron pitch-angle diffusion: resonant scattering by waves vs. nonadiabatic effects. *Annales Geophysicae*, *31*, 1485-1490. doi: 10.5194/angeo-31-1485-2013
- Berube, D., Moldwin, M. B., & Ahn, M. (2006). Computing magnetospheric mass density from field line resonances in a realistic magnetic field geometry. *J. Geophys. Res. (Space Physics)*, *111*, A08206. doi: 10.1029/2005JA011450
- Blake, J. B., Carranza, P. A., Claudepierre, S. G., Clemmons, J. H., Crain, W. R., Dotan, Y., ... Zakrzewski, M. P. (2013, November). The Magnetic Electron Ion Spectrometer (MagEIS) Instruments Aboard the Radiation Belt Storm Probes (RBSP) Spacecraft. *Space Sci. Rev.*, *179*, 383-421. doi: 10.1007/s11214-013-9991-8
- Boyd, A. J., Green, J. C., O'Brien, T. P., & Claudepierre, S. G. (2023). Specifying high altitude electrons using low-altitude LEO systems: Updates to the SHELLS model. *Space Weather*, *21*.

- Boynton, R. J., Amariutei, O. A., Shprits, Y. Y., & Balikhin, M. A. (2019). The system science development of local time-dependent 40-keV electron flux models for geostationary orbit. *Space Weather*, *17*, 894-906. doi: 10.1029/2018SW002128
- Boynton, R. J., Balikhin, M. A., Sibeck, D. G., Walker, S. N., Billings, S. A., & Ganushkina, N. (2016). Electron flux models for different energies at geostationary orbit. *Space Weather*, *14*, 840-860. doi: 10.1002/2016SW001506
- Boynton, R. J., Mourenas, D., & Balikhin, M. A. (2017, November). Electron Flux Dropouts at $L \sim 4.2$ From Global Positioning System Satellites: Occurrences, Magnitudes, and Main Driving Factors. *Journal of Geophysical Research (Space Physics)*, *122*, 11. doi: 10.1002/2017JA024523
- Califf, S., Zhao, H., Gkioulidou, M., Manweiler, J. W., Mitchell, D. G., & Tian, S. (2022, February). Multi-Event Study on the Connection Between Subauroral Polarization Streams and Deep Energetic Particle Injections in the Inner Magnetosphere. *Journal of Geophysical Research (Space Physics)*, *127*(2), e2021JA029895. doi: 10.1029/2021JA029895
- Chen, Y., Carver, M. R., Morley, S. K., & Hoover, A. S. (2021). Determining Ionizing Doses in Medium Earth Orbits Using Long-Term GPS Particle Measurements. *2021 IEEE Aerospace Conference (50100)*, 1-21. doi: 10.1109/AERO50100.2021.9438516
- Claudepierre, S. G., Blake, J. B., Boyd, A. J., Clemmons, J. H., Fennell, J. F., Gabrielse, C., ... Turner, D. L. (2021). The Magnetic Electron Ion Spectrometer: A Review of On-Orbit Sensor Performance, Data, Operations, and Science. *Space Science Reviews*, *217*, 80. doi: 10.1007/s11214-021-00855-2
- ELFIN. (2024). Electron Losses and Fields Investigation (ELFIN) Data Archive, UCLA, USA. [dataset]. <https://data.elfin.ucla.edu/>.
- Gabrielse, C., Angelopoulos, V., Harris, C., Artemyev, A., Kepko, L., & Runov, A. (2017, May). Extensive electron transport and energization via multiple, localized dipolarizing flux bundles. *J. Geophys. Res. (Space Physics)*, *122*, 5059-5076. doi: 10.1002/2017JA023981
- Gannon, J. L., Li, X., & Heynderickx, D. (2007, May). Pitch angle distribution analysis of radiation belt electrons based on Combined Release and Radiation Effects Satellite Medium Electrons A data. *J. Geophys. Res. (Space Physics)*, *112*, 5212. doi: 10.1029/2005JA011565
- Gao, L., Vainchtein, D., Artemyev, A., Gabrielse, C., Runov, A., & Kellerman, A. (2023). Parametrization of energetic ion and electron fluxes in the near-Earth magnetotail. *Journal of Geophysical Research (Space Physics)*, *128*, e2023JA031425. doi: 10.1029/2023JA031425
- Gao, L., Vainchtein, D., Artemyev, A. V., & Zhang, X. J. (2022, August). Statistics of Whistler-Mode Waves in the Near-Earth Plasma Sheet. *Journal of Geophysical Research (Space Physics)*, *127*(8), e30603. doi: 10.1029/2022JA030603
- Gill, P. E., Murray, W., & Wright, M. H. (2020). *Practical optimization*. SIAM, Philadelphia, USA. doi: 10.1137/1.9781611975604
- Gjerloev, J. W. (2012). The SuperMAG data processing technique. *J. Geophys. Res. (Space Physics)*, *117*, A09213. doi: 10.1029/2012JA017683
- Green, A., Li, W., Ma, Q., Shen, X.-C., Bortnik, J., & Hospodarsky, G. B. (2020). Properties of Lightning Generated Whistlers Based on Van Allen Probes Observations and Their Global Effects on Radiation Belt Electron Loss. *Geophys. Res. Lett.*, *47*, e2020GL089584. doi: 10.1029/2020GL089584
- He, Z., Yu, J., Li, K., Liu, N., Chen, Z., & Cui, J. (2021). A Comparative Study on the Distributions of Incoherent and Coherent Plasmaspheric Hiss. *Geophys. Res. Lett.*, *48*, e2021GL092902. doi: 10.1029/2021GL092902
- Horne, R. B., Thorne, R. M., Glauert, S. A., Albert, J. M., Meredith, N. P., & Anderson, R. R. (2005, March). Timescale for radiation belt electron acceleration by whistler mode chorus waves. *J. Geophys. Res. (Space Physics)*, *110*, 3225.

- doi: 10.1029/2004JA010811
- Hua, M., Bortnik, J., Chu, X., & Ma, Q. (2022). Unraveling the Critical Geomagnetic Conditions Controlling the Upper Limit of Electron Fluxes in the Earth's Outer Radiation Belt. *Geophys. Res. Lett.*, *49*, e2022GL101096. doi: 10.1029/2022GL101096
- Hudson, M. K., Elkington, S. R., Li, Z., Patel, M., Pham, K., Sorathia, K., ... Leali, A. (2021). MHD-Test Particles Simulations of Moderate CME and CIR-Driven Geomagnetic Storms at Solar Minimum. *Space Weather*, *19*, e2021SW002882. doi: 10.1029/2021SW002882
- Kanekal, S. G., Baker, D. N., & Blake, J. B. (2001). Multisatellite measurements of relativistic electrons: Global coherence. *J. Geophys. Res. (Space Physics)*, *106*, 29721-29732. doi: 10.1029/2001JA000070
- Kennel, C. F. (1969). Consequences of a magnetospheric plasma. *Reviews of Geophysics and Space Physics*, *7*, 379-419. doi: 10.1029/RG007i001p00379
- Kennel, C. F., & Petschek, H. E. (1966, January). Limit on Stably Trapped Particle Fluxes. *J. Geophys. Res. (Space Physics)*, *71*, 1-28.
- Koochak, Z., & Fraser-Smith, A. C. (2017). An Update on the Centered and Eccentric Geomagnetic Dipoles and Their Poles for the Years 1980–2015. *Earth and Space Science*, *4*, 626-636. doi: 10.1002/2017EA000280
- Lejosne, S., & Mozer, F. S. (2016). Van Allen Probe measurements of the electric drift $E \times B / B^2$ at Arecibo's L=1.4 field line coordinate. *Geophys. Res. Lett.*, *43*(13), 6768-6774. doi: 10.1002/2016GL069875
- Li, W., & Hudson, M. K. (2019, Nov). Earth's Van Allen Radiation Belts: From Discovery to the Van Allen Probes Era. *Journal of Geophysical Research (Space Physics)*, *124*(11), 8319-8351. doi: 10.1029/2018JA025940
- Li, W., Ma, Q., Thorne, R. M., Bortnik, J., Kletzing, C. A., Kurth, W. S., ... Nishimura, Y. (2015, May). Statistical properties of plasmaspheric hiss derived from Van Allen Probes data and their effects on radiation belt electron dynamics. *J. Geophys. Res. (Space Physics)*, *120*, 3393-3405. doi: 10.1002/2015JA021048
- Li, W., Ni, B., Thorne, R. M., Bortnik, J., Green, J. C., Kletzing, C. A., ... Hospodarsky, G. B. (2013, September). Constructing the global distribution of chorus wave intensity using measurements of electrons by the POES satellites and waves by the Van Allen Probes. *Geophys. Res. Lett.*, *40*, 4526-4532. doi: 10.1002/grl.50920
- Li, W., Thorne, R. M., Ma, Q., Ni, B., Bortnik, J., Baker, D. N., ... Claudepierre, S. G. (2014, June). Radiation belt electron acceleration by chorus waves during the 17 March 2013 storm. *J. Geophys. Res. (Space Physics)*, *119*, 4681-4693. doi: 10.1002/2014JA019945
- Lyons, L. R., & Thorne, R. M. (1973, May). Equilibrium structure of radiation belt electrons. *J. Geophys. Res. (Space Physics)*, *78*, 2142-2149. doi: 10.1029/JA078i013p02142
- Ma, D., Chu, X., Bortnik, J., Claudepierre, S. G., Tobiska, W. K., Cruz, A., ... Blake, J. B. (2022). Modeling the Dynamic Variability of Sub-Relativistic Outer Radiation Belt Electron Fluxes Using Machine Learning. *Space Weather*, *20*(08), e2022SW003079. doi: 10.1029/2022SW003079
- Ma, Q., Gu, W., Claudepierre, S. G., Li, W., Bortnik, J., Hua, M., & Shen, X.-C. (2022). Electron Scattering by Very-Low-Frequency and Low-Frequency Waves From Ground Transmitters in the Earth's Inner Radiation Belt and Slot Region. *J. Geophys. Res. (Space Physics)*, *127*, e2022JA030349. doi: 10.1029/2022JA030349
- Ma, Q., Li, W., Thorne, R. M., Bortnik, J., Reeves, G. D., Kletzing, C. A., ... Angelopoulos, V. (2016, December). Characteristic energy range of electron scattering due to plasmaspheric hiss. *J. Geophys. Res. (Space Physics)*, *121*, 11. doi: 10.1002/2016JA023311

- Ma, Q., Mourenas, D., Li, W., Artemyev, A., & Thorne, R. M. (2017, July). VLF waves from ground-based transmitters observed by the Van Allen Probes: Statistical model and effects on plasmaspheric electrons. *Geophys. Res. Lett.*, *44*, 6483-6491. doi: 10.1002/2017GL073885
- Marshall, R. A., & Bortnik, J. (2018, March). Pitch Angle Dependence of Energetic Electron Precipitation: Energy Deposition, Backscatter, and the Bounce Loss Cone. *J. Geophys. Res. (Space Physics)*, *123*, 2412-2423. doi: 10.1002/2017JA024873
- Matsui, H., Torbert, R. B., Spence, H. E., Khotyaintsev, Y. V., & Lindqvist, P.-A. (2013). Revision of empirical electric field modeling in the inner magnetosphere using Cluster data. *J. Geophys. Res. (Space Physics)*, *118*(7), 4119-4134. doi: 10.1002/jgra.50373
- Meredith, N. P., Horne, R. B., Isles, J. D., & Green, J. C. (2016). Extreme energetic electron fluxes in low Earth orbit: Analysis of POES E \geq 30, E \geq 100, and E \geq 300 keV electrons. *Space Weather*, *14*, 136-150. doi: 10.1002/2015SW001348
- Millan, R. M., Cantwell, K., Sample, J. G., Sotirelis, T., McCarthy, M. P., Ukhorskiy, A. Y., ... Merkin, V. G. (2024). Remote Sensing of Magnetospheric Processes from Low Altitude. In *The triennial earth-sun summit (tess)* (Vol. 204, p. 305-06). Retrieved from <https://agu.confex.com/agu/TESS24/prelim.cgi/Paper/1495230>
- Morley, S. K., Brito, T. V., & Welling, D. T. (2018). Measures of model performance based on the log accuracy ratio. *Space Weather*, *16*, 68-88. doi: 10.1002/2017SW001669
- Mourenas, D., Agapitov, O. V., Artemyev, A. V., & Zhang, X. J. (2019). Impact of Significant Time-Integrated Geomagnetic Activity on 2-MeV Electron Flux. *Journal of Geophysical Research (Space Physics)*, *124*(6), 4445-4461. doi: 10.1029/2019JA026659
- Mourenas, D., Agapitov, O. V., Artemyev, A. V., & Zhang, X. J. (2022, August). A Climatology of Long-Duration High 2-MeV Electron Flux Periods in the Outer Radiation Belt. *Journal of Geophysical Research (Space Physics)*, *127*(8), e30661. doi: 10.1029/2022JA030661
- Mourenas, D., Artemyev, A. V., Agapitov, O. V., Krasnoselskikh, V., & Li, W. (2014, December). Approximate analytical solutions for the trapped electron distribution due to quasi-linear diffusion by whistler mode waves. *J. Geophys. Res. (Space Physics)*, *119*, 9962-9977. doi: 10.1002/2014JA020443
- Mourenas, D., Artemyev, A. V., Ripoll, J.-F., Agapitov, O. V., & Krasnoselskikh, V. V. (2012). Timescales for electron quasi-linear diffusion by parallel and oblique lower-band Chorus waves. *J. Geophys. Res. (Space Physics)*, *117*, A06234. doi: 10.1029/2012JA017717
- Mourenas, D., Artemyev, A. V., Zhang, X. J., & Angelopoulos, V. (2023, August). Upper Limit on Outer Radiation Belt Electron Flux Based on Dynamical Equilibrium. *Journal of Geophysical Research (Space Physics)*, *128*(8), e2023JA031676. doi: 10.1029/2023JA031676
- Mourenas, D., Artemyev, A. V., Zhang, X. J., & Angelopoulos, V. (2024, February). Checking Key Assumptions of the Kennel-Petschek Flux Limit With ELFIN CubeSats. *Journal of Geophysical Research (Space Physics)*, *129*(2), e2023JA032193. doi: 10.1029/2023JA032193
- Mourenas, D., Artemyev, A. V., Zhang, X.-J., Angelopoulos, V., Tsai, E., & Wilkins, C. (2021). Electron Lifetimes and Diffusion Rates inferred from ELFIN Measurements at Low Altitude: First Results. *Journal of Geophysical Research: Space Physics*, *126*, e2021JA029757. doi: 10.1029/2021JA029757
- Mourenas, D., Ma, Q., Artemyev, A. V., & Li, W. (2017, April). Scaling laws for the inner structure of the radiation belts. *Geophys. Res. Lett.*, *44*, 3009-3018. doi: 10.1002/2017GL072987
- Mourenas, D., Zhang, X. J., Nunn, D., Artemyev, A. V., Angelopoulos, V., Tsai, E.,

- & Wilkins, C. (2022, May). Short Chorus Wave Packets: Generation Within Chorus Elements, Statistics, and Consequences on Energetic Electron Precipitation. *Journal of Geophysical Research (Space Physics)*, *127*(5), e30310. doi: 10.1029/2022JA030310
- Ni, B., Shprits, Y., Nagai, T., Thorne, R., Chen, Y., Kondrashov, D., & Kim, H.-J. (2009). Reanalyses of the radiation belt electron phase space density using nearly equatorial CRRES and polar-orbiting Akebono satellite observations. *J. Geophys. Res. (Space Physics)*, *114*, A05208. doi: 10.1029/2008JA013933
- Olifer, L., Mann, I. R., Claudepierre, S. G., Baker, D. N., Spence, H. E., & Ozeke, L. G. (2022). A Natural Limit to the Spectral Hardness of Worst Case Electron Radiation in the Terrestrial Van Allen Belt. *J. Geophys. Res. (Space Physics)*, *127*, e2022JA030506. doi: 10.1029/2022JA030506
- Ozeke, L. G., Mann, I. R., Murphy, K. R., Jonathan Rae, I., & Milling, D. K. (2014, March). Analytic expressions for ULF wave radiation belt radial diffusion coefficients. *J. Geophys. Res. (Space Physics)*, *119*, 1587-1605. doi: 10.1002/2013JA019204
- Pires de Lima, R., Chen, Y., & Lin, Y. (2020). Forecasting Megaelectron-Volt Electrons Inside Earth's Outer Radiation Belt: PreMeV 2.0 Based on Supervised Machine Learning Algorithms. *Space Weather*, *18*, e2019SW002399. doi: 10.1029/2019SW002399
- Reeves, G. D., Friedel, R. H. W., Larsen, B. A., Skoug, R. M., Funsten, H. O., Claudepierre, S. G., ... Baker, D. N. (2016, Jan). Energy-dependent dynamics of keV to MeV electrons in the inner zone, outer zone, and slot regions. *Journal of Geophysical Research (Space Physics)*, *121*(1), 397-412. doi: 10.1002/2015JA021569
- Remya, B., Lee, K. H., Le, L. C., & Tsurutani, B. T. (2017). Coherency and ellipticity of electromagnetic ion cyclotron waves: Satellite observations and simulations. *J. Geophys. Res. (Space Physics)*, *122*, 3374-3396. doi: 10.1002/2016JA023588
- Roederer, J. G. (1970). *Dynamics of geomagnetically trapped radiation*. Springer, Berlin. doi: 10.1007/978-3-642-49300-3
- Roederer, J. G., & Lejosne, S. (2018). Coordinates for Representing Radiation Belt Particle Flux. *J. Geophys. Res. (Space Physics)*, *123*, 1381-1387. doi: 10.1002/2017JA025053
- Ross, J. P. J., Glauert, S. A., Horne, R. B., Watt, C. E. J., & Meredith, N. P. (2021, December). On the Variability of EMIC Waves and the Consequences for the Relativistic Electron Radiation Belt Population. *Journal of Geophysical Research (Space Physics)*, *126*(12), e29754. doi: 10.1029/2021JA029754
- Schulz, M., & Lanzerotti, L. J. (1974). *Particle diffusion in the radiation belts*. Springer, New York. doi: 10.1007/978-3-642-65675-0
- Selesnick, R. S., & Blake, J. B. (2002). Relativistic electron drift shell splitting. *J. Geophys. Res. (Space Physics)*, *107*(A9), SMP27-1-SMP27-10. doi: 10.1029/2001JA009179
- Selesnick, R. S., Looper, M. D., & Albert, J. M. (2004, nov). Low-altitude distribution of radiation belt electrons. *Journal of Geophysical Research (Space Physics)*, *109*(A11), A11209. doi: 10.1029/2004JA010611
- Selesnick, R. S., Su, Y.-J., & Blake, J. B. (2016). Control of the innermost electron radiation belt by large-scale electric fields. *J. Geophys. Res. (Space Physics)*, *121*, 8417-8427. doi: 10.1002/2016JA022973
- Shane, A. D., Marshall, R. A., Claudepierre, S. G., & Pettit, J.-M. (2023). Electron Lifetimes Measured at LEO: Comparison With RBSP Estimates and Pitch Angle Resolved Lifetimes. *J. Geophys. Res. (Space Physics)*, *128*, e2023JA031679. doi: 10.1029/2023JA031679
- Shi, R., Summers, D., Ni, B., Fennell, J. F., Blake, J. B., Spence, H. E., & Reeves, G. D. (2016, February). Survey of radiation belt energetic electron pitch

- angle distributions based on the Van Allen Probes MagEIS measurements. *Journal of Geophysical Research (Space Physics)*, *121*(2), 1078-1090. doi: 10.1002/2015JA021724
- Shi, X., Artemyev, A., Zhang, X.-J., Mourenas, D., An, X., & Angelopoulos, V. (2024, January). Properties of Intense H-Band Electromagnetic Ion Cyclotron Waves: Implications for Quasi-Linear, Nonlinear, and Nonresonant Wave-Particle Interactions. *Journal of Geophysical Research (Space Physics)*, *129*(1), e2023JA032179. doi: 10.1029/2023JA032179
- Shprits, Y. Y., Thorne, R. M., Friedel, R., Reeves, G. D., Fennell, J., Baker, D. N., & Kanekal, S. G. (2006, November). Outward radial diffusion driven by losses at magnetopause. *J. Geophys. Res. (Space Physics)*, *111*, 11214. doi: 10.1029/2006JA011657
- Sicard, A., Boscher, D., Bourdarie, S., Lazaro, D., Standarovski, D., & Ecoffet, R. (2018). GREEN: the new Global Radiation Earth ENvironment model (beta version). *Annales Geophysicae*, *36*, 953-967. doi: 10.5194/angeo-36-953-2018
- Simms, L. E., Engebretson, M. J., Rodger, C. J., Dimitrakoudis, S., Mann, I. R., & Chi, P. J. (2021). The Combined Influence of Lower Band Chorus and ULF Waves on Radiation Belt Electron Fluxes at Individual L-Shells. *J. Geophys. Res. (Space Physics)*, *126*, e2020JA028755. doi: 10.1029/2020JA028755
- Simms, L. E., Ganushkina, N. Y., Van der Kamp, M., Balikhin, M., & Liemohn, M. W. (2023). Predicting Geostationary 40–150 keV Electron Flux Using ARMAX (an Autoregressive Moving Average Transfer Function), RNN (a Recurrent Neural Network), and Logistic Regression: A Comparison of Models. *Space Weather*, *21*, e2022SW003263. doi: 10.1029/2022SW003263
- Smirnov, A. G., Berrendorf, M., Shprits, Y. Y., Kronberg, E. A., Allison, H. J., Aseev, N. A., ... Effenberger, F. (2020, November). Medium Energy Electron Flux in Earth's Outer Radiation Belt (MERLIN): A Machine Learning Model. *Space Weather*, *18*(11), e02532. doi: 10.1029/2020SW002532
- Summers, D., Thorne, R. M., & Xiao, F. (1998, September). Relativistic theory of wave-particle resonant diffusion with application to electron acceleration in the magnetosphere. *J. Geophys. Res. (Space Physics)*, *103*, 20487-20500. doi: 10.1029/98JA01740
- SUPERMAG. (2024). Geomagnetic Indices at the SuperMag Data Archive. [dataset]. <https://supermag.jhuapl.edu/indices/>.
- Thorne, R. M., Li, W., Ni, B., Ma, Q., Bortnik, J., Chen, L., ... Kanekal, S. G. (2013, December). Rapid local acceleration of relativistic radiation-belt electrons by magnetospheric chorus. *Nature*, *504*, 411-414. doi: 10.1038/nature12889
- Thébault, E., Finlay, C. C., Alken, P., Beggan, C. D., Canet, E., Chulliat, A., ... Schachtschneider, R. (2015). Evaluation of candidate geomagnetic field models for IGRF-12. *Earth, Planets and Space*, *67*, 112. doi: 10.1186/s40623-015-0273-4
- Tsai, E., Palla, A., Norris, A., King, J., Russell, C., Ye, S., ... Angelopoulos, V. (2024). Remote Sensing of Electron Precipitation Mechanisms Enabled by ELFIN Mission Operations and ADCS Design. *Engineering Archive*. doi: 10.31224/3487
- Tu, W., Cunningham, G. S., Chen, Y., Morley, S. K., Reeves, G. D., Blake, J. B., ... Spence, H. (2014, March). Event-specific chorus wave and electron seed population models in DREAM3D using the Van Allen Probes. *Geophys. Res. Lett.*, *41*, 1359-1366. doi: 10.1002/2013GL058819
- VAN ALLEN PROBES. (2024). Van Allen Probes MagEIS electron flux data (REL03 L2), New Mexico Consortium, USA. [dataset]. https://rbsp-ect.newmexicoconsortium.org/data_pub/rbspa/mageis.
- Walt, M. (1994). *Introduction to geomagnetically trapped radiation*. Cambridge University Press, Cambridge, UK. doi: 10.1017/CBO9780511524981

- Wong, J.-M., Meredith, N. P., Horne, R. B., Glauert, S. A., & Ross, J. P. J. (2022). Electron Diffusion by Magnetosonic Waves in the Earth's Radiation Belts. *J. Geophys. Res. (Space Physics)*, *127*, e2021JA030196. doi: 10.1029/2021JA030196
- Yando, K., Millan, R. M., Green, J. C., & Evans, D. S. (2011). A Monte Carlo simulation of the NOAA POES Medium Energy Proton and Electron Detector instrument. *J. Geophys. Res. (Space Physics)*, *116*, A10231. doi: 10.1029/2011JA016671
- Young, S. L., Denton, R. E., Anderson, B. J., & Hudson, M. K. (2002, June). Empirical model for μ scattering caused by field line curvature in a realistic magnetosphere. *J. Geophys. Res. (Space Physics)*, *107*, 1069. doi: 10.1029/2000JA000294
- Zhang, X. J., Agapitov, O., Artemyev, A. V., Mourenas, D., Angelopoulos, V., Kurth, W. S., ... Hospodarsky, G. B. (2020, October). Phase Decoherence Within Intense Chorus Wave Packets Constrains the Efficiency of Nonlinear Resonant Electron Acceleration. *Geophys. Res. Lett.*, *47*(20), e89807. doi: 10.1029/2020GL089807
- Zhang, X.-J., Angelopoulos, V., Artemyev, A., Mourenas, D., Agapitov, O., Tsai, E., & Wilkins, C. (2023, January). Temporal Scales of Electron Precipitation Driven by Whistler-Mode Waves. *Journal of Geophysical Research (Space Physics)*, *128*(1), e2022JA031087. doi: 10.1029/2022JA031087
- Zhang, X.-J., Angelopoulos, V., Mourenas, D., Artemyev, A., Tsai, E., & Wilkins, C. (2022, May). Characteristics of Electron Microburst Precipitation Based on High-Resolution ELFING Measurements. *Journal of Geophysical Research (Space Physics)*, *127*(5), e30509. doi: 10.1029/2022JA030509
- Zhang, X.-J., Artemyev, A., Angelopoulos, V., Tsai, E., Wilkins, C., Kasahara, S., ... Matsuoka, A. (2022, March). Superfast precipitation of energetic electrons in the radiation belts of the Earth. *Nature Communications*, *13*, 1611. doi: 10.1038/s41467-022-29291-8
- Zhang, X. J., Mourenas, D., Artemyev, A. V., Angelopoulos, V., Kurth, W. S., Kletzing, C. A., & Hospodarsky, G. B. (2020, August). Rapid Frequency Variations Within Intense Chorus Wave Packets. *Geophys. Res. Lett.*, *47*(15), e88853. doi: 10.1029/2020GL088853
- Zhao, H., Li, X., Blake, J. B., Fennell, J. F., Claudepierre, S. G., Baker, D. N., ... Malaspina, D. M. (2014). Characteristics of pitch angle distributions of hundreds of keV electrons in the slot region and inner radiation belt. *J. Geophys. Res. (Space Physics)*, *119*, 9543-9557. doi: 10.1002/2014JA020386
- Zheng, D. J., Ganushkina, N. Y., Jiggins, P., Jun, I., Meier, M., Minow, J. I., ... Kuznetsova, M. M. (2019). Space radiation and plasma effects on satellites and aviation: Quantities and metrics for tracking performance of space weather environment models. *Space Weather*, *17*, 1384-1403. doi: 10.1029/2018SW002042